PhotoniX Life

Open Access
PhotoniX Life (2026)1:5
https://doi.org/10.3724/PXLIFE.2025-0016

Review

Raman microscopy unmixed: Technical advances, bio-orthogonal tags, and applications in life sciences

Erick Alvarado, Zhi Li, Yajuan Li AND Lingyan Shi*

Shu Chien-Gene Lay Department of Bioengineering, University of California San Diego, La Jolla CA 92093, USA
** Corresponding author (email: l2shi@ucsd.edu)*

Received 30 October 2025; accepted 12 March 2026; published online 31 March 2026

Abstract Raman microscopy has emerged as a transformative tool in chemical biology, enabling non-invasive, label-free visualization of biological processes with molecular specificity. This review aims to provide an overview of current Raman microscopy techniques—spanning spontaneous and coherent Raman modalities—and their applications in bioimaging. We outline the core technological advancements driving these techniques, including improvements in spatial, temporal, and spectral resolution, as well as innovations in multiplex imaging and volumetric capabilities. Aspiring to bridge gaps between spectroscopists and biologists, this review highlights the critical applications of Raman microscopy, such as cell metabolism studies, disease progression diagnostics, and tissue mapping, while also exploring emerging technologies like quantum light sources and time-resolved Raman microscopy. Ultimately, this review seeks to foster an appreciation for the evolving capabilities of Raman systems and their potential to enable unprecedented insight into complex biological processes, promoting cross-disciplinary collaboration and innovation in chemical biology.

Keywords Raman, bioimaging, microscopy, spectroscopy, hyperspectral, multimodal

1. Introduction

Originally discovered in 1928 by Raman et al. [1], Raman scattering is an inelastic scattering process of light when it interacts with matter, in which the energy of scattering light is reduced by vibrational modes of chemical bonds in the matter. In the case of biological matter, these vibrations are associated with various chemical bonds constituting the sample of interest (Table 1) [2]. Mechanistically, the process describes the energy transfer between a subpopulation of photons constituting the laser light source and these molecular vibrations, or other excitations, in the sample under analysis. These vibrational modes can either absorb energy from the photon or transfer energy to the photon, lowering or raising the energy of the incident photon upon scattering through the sample. This basic phenomenon and its chemical bond-specific pathways underpin the entire field of Raman microscopy [3].

The different processes and states of Raman scattering are commonly illustrated by using an energy level diagram (Figure 1). Rayleigh scattering describes the instance where light elastically scatters through a given material. The energy rises to that of the incident photon and falls back to the ground state upon scattering through the medium. In the case where a portion of energy is absorbed by a molecular vibrational mode, the photon exits the medium with a lower energy, or longer wavelength, in a process called Stokes scattering. Complementarily, when a molecular vibrational mode transfers its energy to an incident photon, it exits the medium with a higher energy, or shorter wavelength, in a process called anti-Stokes scattering (Figure 1a). These Stokes and anti-Stokes Raman shifts have guided the focus for a variety of specialized microscopy schemes [4,5].

1.1 Spontaneous Raman scattering

In spontaneous Raman spectroscopy, a monochromatic light source is used to induce Raman scattering. For detection, a spectrophotometer is utilized to acquire Raman-shifted photons across a broad range of interactions with various vibrational modes within the sample. Since this approach relies on the intrinsic efficiency for a given sample to induce inelastic scattering, it is also the approach with the longest history of utility in the field. The primary strength of this technique is its ability to collect a broad spectrum of Raman shifts identified in a single shot through a spectrally dispersed spectrometric detection scheme. Beyond this, the linear nature of the process achieves the highest theoretical spectral resolution for Raman shift-associated peaks in the collected spectrum of biochemical analytes [6].

However, the signal strength detected through spontaneous Raman is limited by the efficiency of specific biomolecules, existing at varying concentrations, to inelastically scatter light. Given that these efficiencies are directly tied to molecular scattering cross sections, the detectable concentrations of target analytes are severely limited through spontaneous Raman techniques [7]. While this quality allows for natural quantitative imaging, i.e., signal intensity directly correlating with biochemical analyte concentrations, it is also the primary bottleneck in the

© The Author(s) 2026. This is an Open Access article distributed under the CC BY-NC-ND license (https://creativecommons.org/licenses/by-nc-nd/4.0/).

Table 1 Wavenumber ranges of Raman active biochemical-associated molecular vibrations [2]

Wavenumber range (cm^{-1})	Vibrational mode	Compound functionality
3,400–3,330	Antisymmetric NH_2 stretch	Primary amines
3,380–3,340	OH stretch	Aliphatic alcohols
3,355–3,325	Antisymmetric NH_2 stretch	Primary amides
3,350–3,300	NH stretch	Secondary amines
3,335–3,300	C≡CH stretch	Alkyl acetylenes
3,300–3,250	Symmetric NH_2 stretch	Primary amines
3,310–3,290	NH stretch	Secondary amides
3,190–3,145	Symmetric NH_2 stretch	Primary amides
3,100–3,000	Aromatic CH stretch	Benzene derivatives
3,095–3,070	Antisymmetric = CH_2 stretch	C=CH_2 derivatives
3,062	CH stretch	Benzene
3,057	Aromatic CH stretch	Alkyl benzenes
3,040–3,000	CH stretch	C=CHR derivatives
3,026	Symmetric = CH_2 stretch	Ethylene (gas)
2,990–2,980	Symmetric = CH_2 stretch	C=CH_2 derivatives
2,969–2,965	Antisymmetric CH_3 stretch	n-Alkanes
2,929–2,912	Antisymmetric CH_3 stretch	n-Alkanes
2,884–2,883	Symmetric CH_3 stretch	n-Alkanes
2,861–2,849	Symmetric CH_2 stretch	n-Alkanes
2,850–2,700	CHO group	Aliphatic aldehydes
2,590–2,560	SH stretch	Thiols
2,316–2,233	C≡C stretch	R–C≡C–CH_3
2,301–2,231	C≡C stretch	R–C≡C–R’
2,300–2,250	Pseudoantisymmetric N=C=O stretch	Isocyanates
2,161–2,134	N≡C stretch	Aliphatic isonitriles
2,160–2,100	C≡C stretch	Alkyl alkynes
2,156–2,140	C≡N stretch	Alkyl thiocyanates
1,820	Symmetric C=O stretch	Acetic anhydride
1,810–1,788	C=O stretch	Acid halides
1,805–1,799	Symmetric C=O stretch	Noncyclic anhydrides
1,770–1,730	C=O stretch	Halogenated aldehydes
1,743–1,729	C=O stretch	Cationic α-amino acids
1,725–1,700	C=O stretch	Aliphatic ketones
1,689–1,644	C=C stretch	Monofluoroalkenes
1,686–1,636	Amide I band	Primary amides (solids)
1,680–1,665	C=C stretch	Tetraalkyl ethylenes
1,678–1,664	C=C stretch	Trialkyl ethylenes
1,676–1,665	C=C stretch	*trans*-dialkyl ethylenes
1,670–1,630	Amide I band	Tertiary amides
1,666–1,652	C=N stretch	Ketoximes
1,665–1,650	C=N stretch	Semicarbazones
1,663–1,636	Symmetric C=N stretch	Aldazines, ketazines
1,660–1,654	C=C stretch	*cis*-dialkyl ethylenes
1,660–1,650	Amide I band	Secondary amides
1,660–1,649	C=N stretch	Aldoximes
1,660–1,610	C=N stretch	Hydrazones
1,658–1,644	C=C stretch	$R_2C=CH_2$
1,654–1,649	Symmetric C=O stretch (cyclic dimer)	Carboxylic acids
1,652–1,642	C=N stretch	Thiosemicarbazones
1,650–1,590	NH_2 scissors	Primary amines
1,649–1,625	C=C stretch	Alkyl derivatives
1,648–1,640	N=O stretch	Alkyl nitrites
1,648–1,638	C=C stretch	H_2C=CHR
1,634–1,622	Antisymmetric NO_2 stretch	Alkyl nitrates
1,630–1,550	Ring stretches (doublet)	Benzene derivatives
1,620–1,540	Three or more coupled C=C stretches	Polyenes
1,616–1,571	C=C stretch	Chloroalkenes
1,596–1,547	C=C stretch	Bromoalkenes
1,581–1,465	C=C stretch	Iodoalkenes
1,560–1,550	Antisymmetric NO_2 stretch	Primary nitroalkanes
1,555–1,550	Antisymmetric NO_2 stretch	Secondary nitroalkanes
1,545–1,535	Antisymmetric NO_2 stretch	Tertiary nitroalkanes
1,515–1,490	Ring stretch	2-Furfuryl group
1,480–1,470	OCH_3, OCH_2 deformations	Aliphatic ethers
1,473–1,446	CH_3, OCH_2 deformations	n-Alkanes
1,466–1,465	CH_3 deformation	n-Alkanes
1,450–1,400	Pseudosymmetric N=C=O	Isocyanates
1,443–1,398	Ring stretch	2-substituted thiophenes
1,440–1,340	Symmetric $CO2^-$ stretch	Carboxylate ions
1,415–1,400	Symmetric $CO2^-$ stretch	Dipolar and anionic α -amino acids
1,415–1,385	Ring stretch	Anthracenes
1,395–1,380	Symmetric NO_2 stretch	Primary nitroalkanes
1,390–1,370	Ring stretch	Naphthalenes
1,385–1,368	CH_3 symmetric deformation	n-Alkanes
1,375–1,360	Symmetric NO_2 stretch	Secondary nitroalkanes
1,355–1,345	Symmetric NO_2 stretch	Tertiary nitroalkanes
1,350–1,330	CH deformation	Isopropyl group
1,320	Ring vibration	1,1-dialkyl cyclopropanes
1,314–1,290	In-plane CH deformation	*trans*-dialkyl ethylenes
1,310–1,250	Amide III band	Secondary amides
1,310–1,175	CH_2 twist and rock	n-Alkanes
1,305–1,295	CH_2 in-phase twist	n-Alkanes
1,300–1,280	CC bridge bond stretch	Biphenyls
1,282–1,275	Symmetric NO_2 stretch	Alkyl nitrates
1,280–1,240	Ring stretch	Epoxy derivatives
1,270–1,251	In-plane CH deformation	*cis*-dialkyl ethylenes
1,230–1,200	Ring vibration	Paradisubstituted benzenes
1,220–1,200	Ring vibration	Mono- and 1,2-dialkyl cyclopanes
1,205	C_6H_5–C vibration	Alkyl benzenes

(*Continued*)

Wavenumber range (cm^{-1})	Vibrational mode	Compound functionality
1,196–1,188	Symmetric SO_2 stretch	Alkyl sulfates
1,172–1,165	Symmetric SO_2 stretch	Alkyl sulfonates
1,150–950	CC stretches	n-Alkanes
1,145–1,125	Symmetric SO_2 stretch	Dialkyl sulfones
1,130–1,100	Symmetric C=C=C stretch	Allenes
1,070–1,040	S=O stretch	Aliphatic sulfoxides
1,060–1,020	Ring vibration	Orthodiubstituted benzenes
1,040–990	Ring vibration	Pyrazoles
1,030–1,015	In-plane CH deformation	Monosubstituted benzenes
1,030–1,010	Trigonal ring breathing	3-substituted pyridines
1,030	Trigonal ring breathing	Pyridine
1,029	Ring breathing	Trimethylene oxide
1,010–990	Trigonal ring breathing	Mono-, meta-, and 1,3,5-substituted benzenes
1,000–985	Trigonal ring breathing	2- and 4-substituted pyridines
933	Ring vibration	Alkyl cyclobutanes
930–830	Symmetric COC stretch	Aliphatic ethers
905–837	CC skeletal stretch	n-Alkanes
900–890	Ring vibration	Alkyl cyclopentanes
900–850	Symmetric CNC stretch	Secondary amines
851–840	Pseudosymmetric CON stretch	O-Alkyl hydroxylamines
835–749	Skeletal stretch	Isopropyl group
830–720	Ring vibration	Paradisubstituted benzenes
825–820	C_3O skeletal stretch	Secondary alcohols
818	Ring breathing	Tetrahydropyran
785–700	Ring vibration	Alkyl cyclohexanes
760–730	C_4O skeletal stretch	Tertiary alcohols
760–650	Symmetric skeletal stretch	tert-Butyl group
740–585	CS stretch (1 or more bands)	Alkyl sulfides
735–690	C=S stretch	Thiomades, thioureas (solid)
730–720	CCl stretch	Primary chloroalkanes
715–620	CS stretch	Dialkyl disulfides
690–650	Pseudosymmetric N=C=S	Alkyl isothiocyanates
660–650	CCl stretch, P_H conformation	Primary chloroalkanes
655–640	CBr stretch, Pc conformation	Primary bromoalkanes
630–615	Ring deformation	Monosubstituted benzenes
615–605	CCl stretch, S_{HH} conformation	Secondary chloroalkanes
610–590	Cl stretch, P_c conformation	Primary iodoalkanes
570–560	CCl stretch, T_{HHH} conformation	Tertiary chloroalkanes conformation
565–560	CBr stretch, P_H conformation	Primary bromoalkanes
540–535	CBr stretch, S_{HH} conformation	Secondary bromoalkanes
525–510	SS stretch	Dialkyl disulfides
520–510	CBr stretch, T_{HHH} conformation	Tertiary bromoalkanes
510–500	CI stretch, P_H conformation	Primary iodoalkanes
510–480	SS stretch	Dialkyl trisulfides
495–485	CI stretch, S_{HH} conformation	Secondary iodoalkanes
495–485	CI stretch, T_{HHH} conformation	Tertiary iodoalkanes
484–475	Skeletal deformation	Dialkyl dialkynes
425–150	Chain expansion	n-Alkanes
355–335	Skeletal deformation	Monoalkyl alkynes
200–160	Skeletal deformation	Aliphatic nitriles

application of the technique in imaging less abundant biochemical species. To address these limitations, a variety of coherent Raman imaging schemas have been developed with the goal of amplifying these signals through nonlinear excitation.

1.2 Coherent Raman scattering

While spontaneous Raman scattering can readily achieve chemical-specific contrast, its weak cross sections significantly limits the sensitivity and imaging speed. CRS techniques overcome these limits by driving molecular vibrations coherently through synchronized laser excitation and probe fields. Coherent schemes greatly enhance the signal-to-noise ratio (SNR), enabling detection of lower analyte concentrations at faster acquisition rates. CRS encompasses two major modalities, coherent anti-Stokes Raman scattering (CARS) and stimulated Raman scattering (SRS), each leveraging nonlinear optical interactions to amplify Raman signals with distinct differences in detection schemes, background rejection, and quantitative linearity with biochemical concentrations. Together, they provide options for rapid, label-free chemical imaging of biological specimens with high sensitivity and molecular specificity.

(1) Coherent anti-Stokes Raman scattering. CARS is a third-order nonlinear (four-wave-mixing) process that coherently drives a chosen vibration using a pump beam (ω_p) and a Stokes beam (ω_s) whose frequency difference matches a molecular vibrational frequency $\left(\Omega = \omega_p - \omega_s\right)$. A probe field ($\omega_{pr}$) scatters from the induced vibrational coherence to generate anti-Stokes photons at

$$\omega_{AS} = \omega_{pr} + \Omega\left(\text{degenerate “pump-as-probe” gives } \omega_{AS} = 2\omega_p - \omega_s\right). \quad (1)$$

Because the fields add coherently and obey phase matching, the anti-Stokes emission is highly directional and efficiently collected. The resonant CARS field scales linearly with the number of Raman-active oscillators (N), so the CARS intensity scales ~N^2, providing large enhancements (often quoted as ~10^3–10^6 over spontaneous Raman under comparable conditions). The main limitation is the nonresonant electronic background (the instantaneous χ^3 response), which interferes with the resonant signal and can distort lineshapes (dispersive/phase-shifted pro-

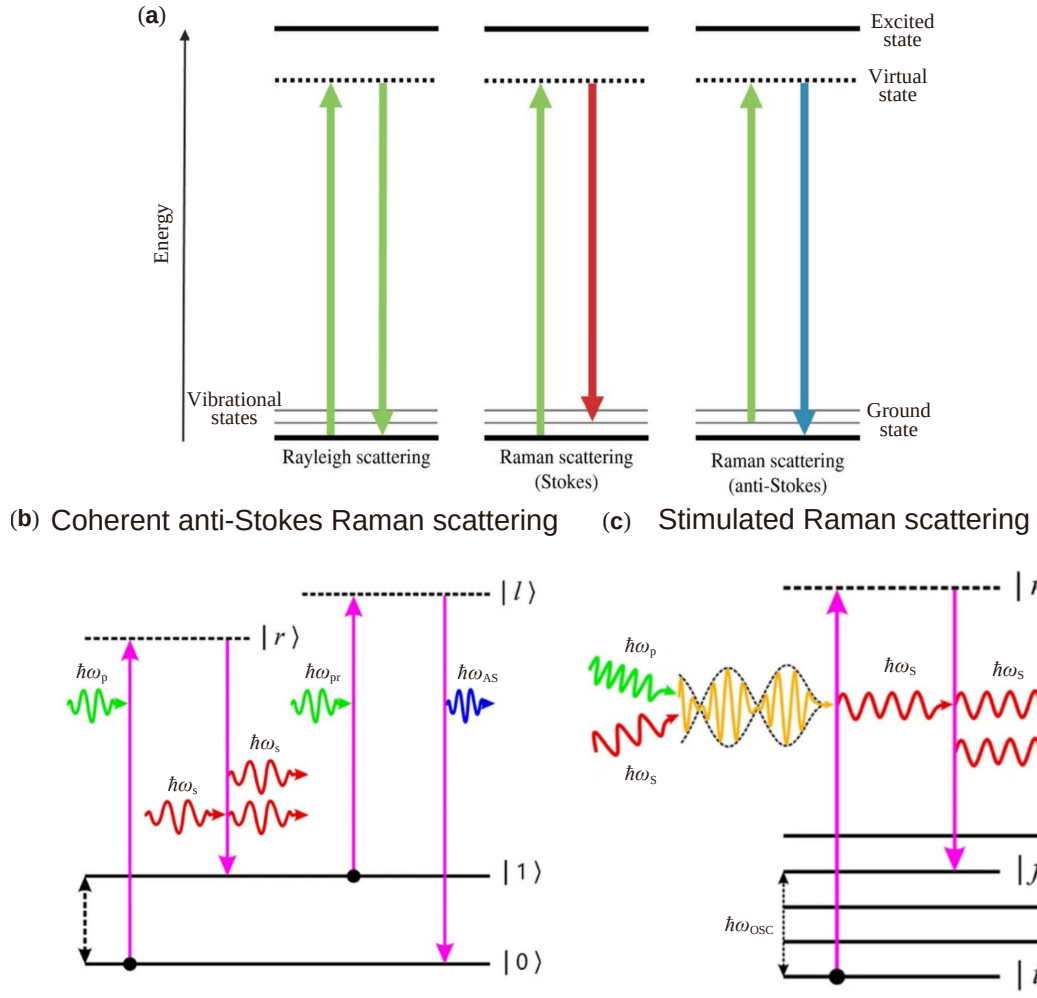


Figure 1 Energy transfer processes in spontaneous and coherent Raman scattering (CRS) microscopy modalities. **a.** Energy level diagram of spontaneous Raman scattering processes. In Stokes Raman scattering, the final vibrational mode energy within the medium is greater than the initial state as the vibrational mode absorbs energy from incident photons. In anti-Stokes Raman scattering, the final vibrational mode energy within the medium is less than the initial state that already carries energy due to thermal excitation from the environment, transferring this energy to photons upon interaction [4]. **b.** Energy level diagram of coherent anti-Stokes Raman scattering (CARS) processes. Through the combination of a 4-wave mixing process utilizing pump, Stokes, probe, and generated anti-Stokes light, CARS coherently amplifies anti-Stokes Raman signals by generating a coherently maintained population of excited vibrational modes at a target energy dictated by the difference in energy between Pump and Stokes excitation beams. **c.** Energy level diagram of stimulated Raman scattering (SRS) processes. Through a 3-beam process utilizing pump, Stokes, and generated Stokes light, SRS coherently generates Stokes light emission at target molecular vibrational mode energies set by the frequency difference of the exciting pump and Stokes beams. The magnitude of Raman signals is read out from intensity loss and gain fluctuations in the pump and Stokes beams, respectively, as a result of energy transfer to the coherently excited molecular vibrational mode population [5].

files), complicating quantitative spectral interpretation [8,9]. Tight focusing in microscopy relaxes bulk phase-matching constraints, but careful polarization, time/frequency shaping, or epi-detection is often used to mitigate nonresonant contributions.

(2) Stimulated Raman scattering. SRS uses the same pump/Stokes pair to drive the vibrational coherence $\left(\Omega = \omega_p - \omega_s\right)$ but detects intensity transfer between the driving beams rather than newly generated anti-Stokes light (Figure 1). On resonance, the pump experiences stimulated Raman loss (SRL) and the Stokes experiences stimulated Raman gain (SRG). The small fractional change (ΔI) is measured by modulating one beam and using lock-in detection

$$\Delta I \propto N \cdot \sigma \cdot I_p \cdot I_s \tag{2}$$

where N is the concentration of Raman-active molecules, σ is the Raman cross-section, I_p is the pump beam intensity, and I_s is the Stokes beam intensity. Crucially, SRS signal intensity is linearly proportional to concentration ($\propto N$) and, unlike CARS, is free of the χ^3 nonresonant background that distorts spectra, enabling quantitative, background-free Raman imaging [10-12]. Practical parasitic signals (e.g., cross-phase modulation, thermal lensing, two-photon absorption) can appear but are minimized with proper modulation frequency, focusing, and timing.

1.3 Functional readout of Raman imaging

The intrinsic ability of Raman scattering processes to identify specific vibrational excitations within biomolecules underpins

their power in applications to construct an entire spectrum of biomolecule-associated Raman shifts (Table 1). By isolating the response from channels associated with a biomolecule's specific vibrational mode, populations of these molecules can be mapped across the sample. This capability forms the basis for a variety of powerful applications that allow researchers to investigate the molecular underpinnings of biological systems in unprecedented detail [13].

Raman techniques enable a variety of key diagnostic techniques to interrogate biological dynamics. Through intrinsic sensitivity to natural vibrational signatures in a biological sample, the imaging of biomolecular subpopulations is noninvasive in nature. Additionally, the identification of these molecules is label-free, leaving biological dynamics unperturbed by exogenous labeling techniques normally required to identify specific biochemical analytes. These capabilities have produced critical research ranging from pharmacokinetic studies to disease progression, inspiring the development of additional biomolecular techniques to push Raman microscopy's ability for molecular identification even further [14]. Finally, interpreting Raman imaging readouts within the broader landscape of biochemical and functional measurements is essential for selecting appropriate strategies to study biological systems. Guidance on integrating Raman-derived molecular information with complementary imaging and analytical approaches has been reviewed in prior work [15-19].

2. Raman probes

Although Raman microscopy has an intrinsic ability to spectrally identify subcomponents in biological tissues, its application is often limited by the spectral overlap of biochemical signatures and the need for improved sensitivity in complex biological environments. To address these challenges, Raman tags have been developed to enhance the specificity and utility of Raman techniques (Figure 2). These tags enable the segregation of target pathways or analytes that might otherwise be spectrally indistinguishable and facilitate more dynamic imaging of biological processes. By leveraging the unique vibrational signatures of these tags, researchers can achieve higher specificity in visualizing molecular dynamics, tracking metabolic pathways, and probing cellular interactions in real time. Commonly used Raman tags and their applications in bioimaging are introduced below.

2.1 Stable isotope tags

Stable isotope (such as ^{13}C and ^{2}H) labeling is a bio-orthogonal approach to modifying biochemical signatures inside biological media with minimal disruption of the biological system. The approach involves the incorporation of isotope atoms into biological compounds such as DNA, lipids, and proteins and marking them. As illustrated in Figure 2a, the mass change in the biomolecules shifts the vibrational frequencies of the associated bonds within them, granting them a distinct spectral position outside of the generally crowded organic fingerprint region. By dynamically tracking the intensity of these signals, insights into lipid, protein, and DNA metabolism can be garnered.

Stable isotope labelling has been utilized to answer a wide array of questions concerning biological dynamics and applications. For instance, an early example used deuterated amino acids (phenylalanine, tyrosine, and methionine) to label proteins in cell cultures, and imaged protein synthesis using spontaneous Raman spectroscopy [20]. Integrating a coherent Raman schema and deuterium oxide as a metabolic tracer in animal models, the metabolic dynamics of de novo lipogenesis, protein synthesis, and DNA production were tracked [21]. In application of Raman spectroscopy to bacterial cell sorting, Razi et al. [22] used deuterium oxide (D_2O) and carbon-13 (^{13}C) isotope labels to distinguish between labeled and unlabeled bacteria, allowing for sorting based on metabolic activity rate through a microfluidic device. Another study utilized D_2O labeling to track the metabolic activity of bacteria in response to antibiotic treatment, which enabled differentiation between sensitive, tolerant, and resistant bacterial subpopulations [23]. Using D_2O labeling to image metabolic dynamics in the hyphal tips of the *Aspergillus nidulans* fungi, Yasuda et al. [24] imaged the spatial distribution of glucose uptake and protein synthesis within fungal cell subregions through time-lapse Raman imaging. Yonamine et al. [25] tracked the biogenesis of polysaccharide granules in algal cells by utilizing SRS microscopy in conjunction with ^{13}C labeling to image the growth dynamics of paramylon granules.

2.2 Triple bond vibrational tags

Like stable isotope labeling, the goal of triple bond vibrational tags (such as alkyne) is to move biochemical vibrational signatures normally observed in the vibrational spectrum fingerprint region into the cell-silent region for clearer identification. Triple bond vibrational tagging integrates alkyne or nitrile groups into biomolecules, exhibiting vibrational modes between 1,800–2,800 cm^{-1} (Figure 2b). Unlike stable isotope labeling that can be global or pathway specific in nature, by using deuterated water or glucose that will get incorporated into biomolecules during enzymatic synthesis, triple bond substrates are typically designed to target specific subsets of biochemical analytes. This specificity is in part due to the additional restriction to these substrates by the enzymatic pathways that process alkyl or nitrile chemistry.

A number of studies have used the creative integration of triple bond vibrational tags to investigate targeted phenomena in biological systems. An early characteristic study integrated alkyne-tagged coenzyme Q and 5-ethynyl-2'-deoxyuridine, respectively, with spontaneous Raman microscopy to image their colocalization in lipid membrane structures and dynamics in cell nuclei [26]. Integrating alkyne tagging with SRS, Wei et al. [27] visualized the dynamic incorporation of tagged RNA, proteins, and phospholipids in HeLa cells and neurons. Using terminal alkyne tags incorporated via recombinant DNA technology, Romei et al. [28] studied the local behavior of peptides and protein environments as solvatochromic shifts in Raman frequency in response to local environmental changes. Integrating both stable isotope and triple bond vibrational tag labeling, Bi et al. [29] achieved local environment sensing of phospholipid, DNA, and nucleoside dynamics. The technique used the local environment dependence of the rate of variations in alkyne-associated Raman shifts while the constituent hydrogen atoms were exchanged with deuterium oxide. Fujioka et al. [30] utilized

isotope-edited nitrile tags, attached to enzyme-specific substrates, to achieve multiplexed imaging of enzymatic pathways with additional dynamical information from an enzyme cleavage-dependent Raman activation. de Moliner et al. [31] developed triple bond-tagged sucrose analogues containing alkyne, nitrile, or azide groups for real-time imaging of sucrose uptake and trafficking in plant cells.

2.3 Raman active nanomaterials

An alternative approach to bioorthogonal pathways is the utilization of Raman-active nanomaterials, which act as selective scaffolds to enhance the signal from a particular vibrational mode. This is primarily achieved through the surface-enhanced Raman scattering (SERS) phenomenon from biomolecules adhered to the metallic surfaces (Figure 2c). Mechanistically, this enhancement is generated from localized surface plasmon resonances producing enhanced electromagnetic fields at the surface of metallic nanostructures hosting collectively oscillating conduction electrons upon illumination at resonant wavelengths. Biomolecules positioned within these near-field hot spots experience amplified Raman scattering, yielding orders of magnitude signal enhancement [32]. As shown by Wang et al. [33], the SERS effect can be utilized in the design of analyte-specific tags, which isolate specific vibrational mode signatures by selectively enhancing the electromagnetic field experienced by associated biomolecules. Advances in nanoparticle design, exemplified below, leverage controlled gap geometries, core-shell architectures, and surface functionalization to improve target specificity and multiplexing capability.

Nanoparticle designs can vary in response to biological applications, as demonstrated in recent works. Li et al. [34] used magnetic core nano gapped gold shell nanoparticles (Fe_3O_4@Au) functionalized with antibody-tagged 5,5'-Dithio-bis(2-nitrobenzoic acid) (DTNB) for ultrasensitive Raman detection and magnetic separation of tagged bacterial species. Wang et al. [35] utilized gold nanoparticle scaffolds functionalized with a variety of distinct Raman reporter ligands for multiplex immunophenotyping of cell surface proteomes. In another modification to the core-shell nanoparticle architecture, Li et al. [36] applied gold core nanoparticles with mesoporous silica shells and an embedded mercaptobenzoic acid Raman reporter for detecting inflammatory biomarkers through C-reactive protein and serum amyloid A antibody functionalization. The gap between core and shell structures can also be used to enhance Raman signals from embedded Raman reporters even further with the design of Gap-Enhanced Raman Tags (GERTs). Bao et al. [37] demonstrated this using a dual tag approach with gold core, silica shell nanoparticles with either folate receptor or nontargeted Raman reporters for quantitative diagnosis and 3D imaging of metastatic lymph nodes through folate receptor distributions. Similarly, Zhang et al. [38] achieved multiplexed Raman imaging of single H1299 cells using gap-enhanced nanoparticle Raman tags consisting of a gold core surrounded by a gold shell with an interior gap preloaded with 4-nitrobenzenethiol reporters (Figure 2c).

2.4 Multiplex Raman dyes

Raman tags are excellent at isolating specific biochemical Raman signals spectrally or through signal enhancement. Efforts have been made to push these capabilities even further by expanding the number of individual biochemical species that can be imaged simultaneously through spectral channels spanning the Raman cell silent region. This is typically achieved through either a series of Raman-active organic dyes or nanoparticles functionalized with a variety of Raman reporter ligands (Figure 2d). An early characteristic example of the approach was performed by using gold core and silica shell nanoparticles functionalized with 10 unique Raman reporter molecules. Integrated into a Raman microscopy scheme, the approach successfully imaged the distribution of the nanoparticles throughout mouse tissue samples across the 10 distinct spectral channels with minimal crosstalk [39].

Since this early demonstration, several studies have employed multiplexed Raman paradigms for imaging achievements of increasing sophistication. In application to tumor microenvironment imaging, Yu et al. [40] utilized gold multicore nanoparticle aggregates, housed in a silica shell equipped with one of 5 distinct subpopulations of Raman reporters, to quantitatively image nanoparticle accumulation across the 5 associated spectral channels. Zhao et al. [41] utilized polystyrene nanoparticles, or Raman dots, as a core matrix in which Raman-active small molecule dyes are embedded using a swelling-diffusion technique. The small size and dense volumetric packing of Raman probes within the polystyrene matrix of the particles enabled the fabrication of 6 distinct Raman reporters, based on Carbow dye integration, which exhibited enhanced Raman signals and easy penetration into cellular environments. Functionalization with antibodies compatible with various cytoskeletal proteins and enzymes enabled multiplexed imaging under a SRS microscopy scheme. Later work expanded the palette for Raman dots by incorporating more species of Raman dyes in polystyrene matrices, which enabled multiplexed imaging across 14 unique spectral channels in the Raman cell silent region [42]. Another paradigm to multiplexed imaging utilizes chemically tuned triple bond vibrational tags. Through conjugation of these probes to secondary antibodies, multiplexed imaging of 12 distinct protein markers was achieved in thick tissue sections [43].

2.5 Summary

Collectively, the development of Raman probes portends a trend toward enhancing chemical specificity and sensitivity in biologically complex environments where intrinsic Raman contrast is muddled from various sources. Stable isotope probes provide a minimally perturbative approach for tracking global biosynthetic activity; however, their chemical specificity is limited by their global incorporation within a host downstream biosynthetic pathway, and their signals are relatively weak. In contrast, triple bond vibrational tags provide enhanced molecular specificity by targeting defined substrates utilized in specific enzymatic pathways. However, the limitations of compatibility with alkyne chemistry within host organisms can result in potential perturbation to natural biochemical processes. Raman-active nanomaterials and SERS-based tags achieve orders of magnitude signal enhancement and enable highly multiplexed detection, but they introduce tradeoffs related to quantification, probe heterogeneity, delivery efficiency, and biocompatibility in live systems.

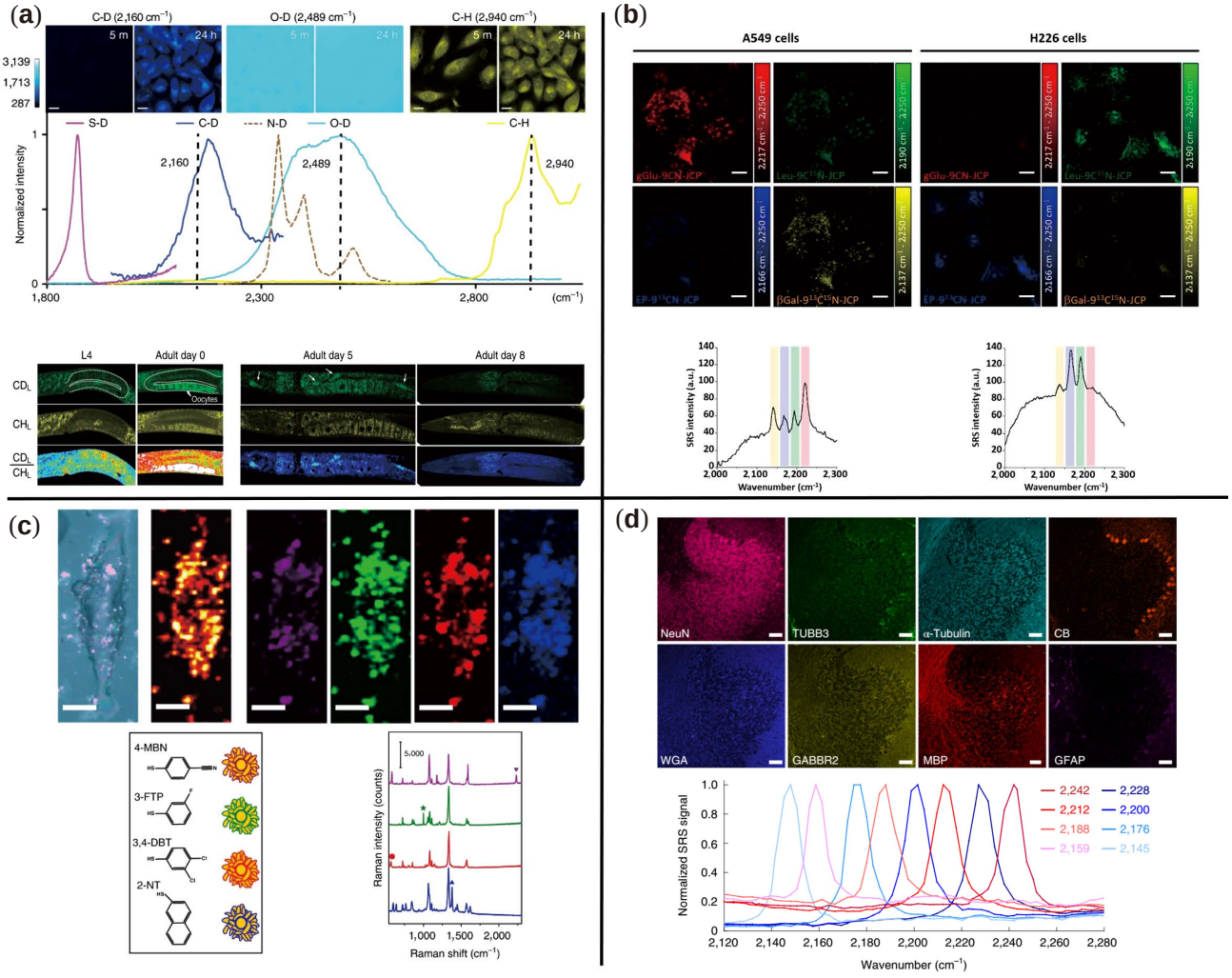


Figure 2 Raman tag approaches to biochemical imaging. **a.** Deuterium oxide labeling. Spectral representation of various X-D bonds generated through biosynthetically incorporated deuterium oxide throughout the cell silent region of Raman spectral acquisition, with specific peaks for deuterium-substituted C-D, O-D, and N-D signals. Imaging across these channels enables selective tracking of de novo synthesis of relevant biological macromolecules (e.g., lipids, DNA, and proteins). Below, lipid turnover rates are determined through ratio metric imaging of lipid and deuterated lipid channels in **c** elegans model system across aging [21]. **b.** Triple bond vibrational tags. Simultaneous multichannel imaging of four enzyme activities in A549 and H226 cells through the incorporation of antibody functionalized nitrile triple bond tags with peaks across the cell silent region of Raman spectral acquisition, as exhibited below [30]. **c.** Nanomaterial Raman tags. Multiplexed Raman imaging of a single H1299 cell through the utilization of gap-enhanced nanoparticle Raman tags functionalized with Raman reporters for target analytes. As shown below, spectral isolation is achieved through selective Raman peak-associated signal amplification through local electric field enhancements from nanoparticle plasmonic resonance phenomena interacting with Raman reporter-associated analytes [38]. **d.** Multiplex Raman dyes. 8 target multiplexed imaging of mouse cerebellum tissue section through the utilization of isotope-variant nitrile bond tags to generate distinct spectral peaks across the entirety of the cell silent region [43].

Common to the majority of these approaches, practical constraints, including probe size, cytotoxicity, tissue penetration, and spectral crowding, produce natural limits on multiplexing potential with increasing depth and spatial resolution. The optimal choice of Raman probe is application-dependent after consideration of tradeoffs surrounding sensitivity, specificity, biological compatibility, and experimental complexity. Open challenges include improving quantitative interpretation across heterogeneous probe distribution, expanding multiplexing capabilities further without sacrificing spectral clarity, and advanced probe designs for even more seamless integration within biological model systems.

3. Applications in biomedical research

3.1 Imaging cellular metabolic activities

The ability of Raman microscopy to visualize the dynamics of specific biomolecules in cell and tissue samples has powerful implications for studies of cellular metabolism processes. Zhang et al. [44] used SRS for *in vivo* high-resolution mapping of glucose metabolism by spectral tracing of deuterium (STRIDE), as C-D bonds progressively incorporated into various macromolecules relying on deuterated glucose substrates, and visualized glucose-derived biosynthesis pathways. Similarly, Borek-Dorosz et al. [45] applied deuterium-labeled glucose to track the integration of

carbon into biomolecular products inside live endothelial cells, identifying the impact of inflammation markers on cellular metabolic activity (Figure 3a). Li et al. [46] used D_2O-probed SRS (DO-SRS) microscopy to investigate the role of lipid metabolism in aging Drosophila. They have visualized and quantified the spatial distribution of lipid turnover rates at subcellular resolution and discovered that high protein and high sugar diets increase lipid turnover while shortening lifespans (Figure 3b). In a recent follow-up study, Li et al. [47] developed the DO-SRS platform further for subcellular identification of metabolites derived from individual isotope-labeled substrates within a multiplexed deuterium-labeled substrate co-labeling platform (SuMMIT-SRS). Focusing on metabolic activity in *Mycobacterium smegmatis* as a model for tuberculosis-related bacteria under antibiotic treatment, Ueno et al. [48] utilized DO-SRS to identify that persistor cells exhibit regular metabolic activity and cell growth even in the presence of antibiotics, disproving a theory positing cell dormancy. In a study investigating the impact of cancer on glycosylation, Kopec et al. [49] mapped glycan, protein, and lipid distributions within cancerous and healthy regions of breast and brain tumor tissue sections through spectral unmixing of glycan-specific peaks from label-free Raman spectra (Figure 3c). Raman-based modalities can also characterize the response of cellular metabolic activity to nanoengineered environments. Li et al. [50] employed DO-SRS and two-photon fluorescence imaging to visualize lipid and protein turnover between HeLa cells on flat and nanopillar substrates *in vitro*.

3.2 Mapping molecular heterogeneity in biological tissues

Capabilities surrounding the imaging of spatial distributions of biochemical subspecies have been showcased in several recent studies. By expanding the library of SERS nanoparticle tags for spatial multiplexing, Eremina et al. [51] explicitly mapped the spatial distribution of 26 distinct biomolecules, including several disease biomarkers, throughout both cultured cancer cells and human tissue samples (Figure 3d). Albro et al. [52] mapped the spatial distribution of glycosaminoglycans, collagen, and water throughout native and engineered cartilage tissues. Taking aim at the limitations of spectral overlap in extracellular matrix-dominated samples, a multivariate curve resolution algorithm was applied to hyperspectral Raman data to disentangle overlapped signals. Chen et al. [53] utilized broadband CARS microscopy in conjunction with stable isotope labeling to map the turnover dynamics of lipid particles in intestinal, epidermal, and gonadal tissue sections in *Caenorhabditis elegans* (*C. elegans*), and revealed lipid particle subpopulations were associated with specific physiological functions in the animal. Ji et al. [54] applied label-free SRS imaging to detect amyloid plaques in Alzheimer's disease progression and differentiated misfolded proteins from normal proteins based on a blue shift of amide I Raman spectra (Figure 3e). The label-free nature of Raman microscopy modalities also enables facile integration with information garnered from other imaging methods. In a multimodal imaging study, Fung et al. [55] applied SRS microscopy to map protein, lipid, and lipid subtype distributions between diabetic and healthy kidney tissues in a label-free manner, revealing spatial biomarkers of diabetic kidney disease progression. Li et al. [56] introduced Raman enhanced delineation of cell atlases in tissues (REDCAT), integrating SRS with immunofluorescent multiplexed imaging, to coregister the spatial distribution of these signals with over 40 antibody-tagged analytes in human lymphoma tissue sections (Figure 3f).

3.3 Detecting molecular changes in diseases

Imaging key biomarkers associated with biochemical pathways of disease progression improves our mechanistic understanding of chronic diseases with implications for translational medicine. Du et al. [57] characterized subcellular lipid metabolism in single melanoma cell lines with varying levels of differentiation, identifying higher de novo fatty acid synthesis in differentiated cells as a metabolic susceptibility for pharmacological targeting (Figure 3g). Using DO-SRS microscopy to investigate lipid accumulation, Li et al. [58] imaged lipid droplet accumulation in mouse hippocampus, fruit fly brain, and human iPSC neuron models of tauopathy progression, identifying lipid metabolism across disease stages (Figure 3h). To investigate the role of cytochrome C in breast cancer development, Abramczyk et al. [59] quantified the redox state and localization of cytochrome C in human breast tissue and cultured cells. They revealed that cancerous ducts exhibit a significant redox imbalance with the reduced form of cytochrome C accumulating in the extracellular matrix, while in healthy cells, cytochrome C is primarily localized within mitochondria in an oxidized form, suggesting metabolic reprogramming through mitochondrial dysfunction with cancer aggressiveness. Li et al. [60] further employed DO-SRS microscopy to distinguish triple-negative breast cancer subtypes by characterizing lipid and protein synthesis pattern-associated markers (Figure 3i). Haessler et al. [61] utilized hyperspectral Raman microscopy data to map the spatial distribution of amyloid plaques, cell nuclei, lipids, and cytochrome C. They found lipid accumulation surrounding amyloid plaques, which suggests a role in driving local toxicity changes with explicit links to mitochondrial dysfunction and associated oxidative stress. Finally, to study the spatial and molecular information of lipid accumulation in non-alcoholic fatty liver disease, Minamikawa et al. [62] successfully visualized the distribution and molecular composition of macro- and micro-vesicular lipid droplets in hepatocytes, identifying the unsaturation degree and cholesterol level in lipid droplet composition.

3.4 Imaging drug delivery in cells and tissues

The biochemical specificity of Raman microscopy techniques presents a powerful tool for imaging the dynamics of pharmacological interventions to disease pathways. Altangerel et al. [63] developed a thermostable Raman interaction profiling (TRIP) technique for low concentration screening of binding between protein-ligand. TRIP was employed on eight protein-ligand systems and generated reproducible Raman measurements. This technique shows potential for high-throughput drug screening and drug development. Tipping et al. [64] utilized the intrinsic alkyne group of dicoidin domain receptor 1 (DDR1) inhibitor 7RH as a Raman tag to investigate real-time pharmacokinetic

uptake of the drug within MCF-7, MDA-MB-231, HCT 116, and A549 cell lines (Figure 3j). In another study focusing on the distribution of lipophilic drugs upon administration, LaLone et al. [65] utilized high-throughput inkjet-printed micro calibration Raman reference standards at varying drug concentrations to quantitatively map drug accumulation and identify their initial isolation in macrophages and subsequent precipitation within lysosomes (Figure 3k). Using alkyne-tagged hyperspectral SRS microscopy, Bae et al. [66] tracked antibiotic penetration into *Staphylococcus aureus* biofilms and revealed nonuniform diffusion limited by strong binding to bacterial cells near the surface. They also visualized the mitochondrial localization and drug uptake dynamics of triphenyl phosphonium (TPP), revealing the influence of membrane potential on TPP uptake [67]. Utilizing a two-channel stimulated Raman microscopy scheme, Lin et al. [68] achieved real-time dynamical insights into the temporal dynamics of dimethyl sulfoxide (DMSO) penetration through a human sweat pore (Figure 3l).

3.5 Summary

From a practical perspective, Raman microscopy offers a unique toolkit for probing biological systems across scales, though its utilization depends strongly on matching imaging techniques to the specific biological question at hand. Specifically, label-free strategies are well-suited for interrogating endogenous metabolic activity and molecular turnover with minimal perturbation in *in vivo* studies. However, without modifications, these methods are inherently limited by common issues including spectral overlap, limited sensitivity for low-abundance molecular species, and usual tradeoffs among spectral resolution, imaging speed, and SNR. In contrast, Raman tag-based strategies provide greatly enhanced sensitivity and multiplexing capacity, realizing the targeted detection of analytes within specific biochemical pathways inaccessible by other means. However, these approaches in biological study are constrained by probe delivery, biological compatibility, quantification accuracy, and heterogeneity in probe distribution. While hyperspectral acquisition and multivariate analysis approaches can provide label-free options to circumvent some of these challenges, these techniques regularly have longer acquisition times and increased photodamage risk. Other challenges of Raman imaging in living organisms include light penetration depth, phototoxicity under prolonged excitation, and translation of high-dimensional Raman data sets into readily identifiable biomarkers. Continued progress in probe design, acquisition strategies, and computational analysis will be needed to expand the range of biological systems and translational contexts where Raman microscopy can be applied.

4. Development of advanced Raman imaging capabilities

4.1 Spontaneous Raman scattering

4.1.1 Challenges and limitations in spontaneous Raman scattering

The limitations of spontaneous Raman microscopy schemes (Figure 4a [69]) stem from the reliance on intrinsic efficiencies for Raman scattering processes in biological media under linear excitation. Quantitatively, the intrinsic Raman effect is very weak, with only ~1 in 10 million photons within the exciting laser source undergoing inelastic scattering, which results in low SNR. Within the context of biomedical imaging, this makes the identification of low-concentration biochemical subpopulations difficult and even limits the resolvable accumulations of biomolecules presenting sufficient signals for detection. Additionally, signals from species with intrinsic sensitivity for other nonlinear effects (such as second harmonic generation or multiphoton fluorescence) may generate stronger signals than Raman scattering, further obscuring Raman peaks. Weak Raman signals also experience interference from shot noise and low-frequency laser intensity noise, while mechanical drift and stray light can further degrade signal stability. To acquire sufficient signals for imaging, exposure times can be extended at the expense of limiting the imaging speed. Alternatively, higher power laser sources can be used, but with possible photodamage to biological tissue samples. Volumetric imaging applications are limited under a linear schema since initially weak signals continue to attenuate from elastic scattering and absorption as focal points are directed deeper into tissue samples. Inspired by these limitations, several creative solutions have been developed to improve signal enhancement, imaging speed, volumetric imaging ability, and spatial resolution through spontaneous Raman microscopy schemes (Figure 5) [70].

4.1.2 Enhancing the signal-to-noise ratio of Raman scattering

In spontaneous Raman microscopy, the SNR enhancement is achieved by selectively amplifying Raman signals relative to background contributions produced from autofluorescence, shot noise, and laser intensity fluctuations. One direction of progress centers on the optimization of SERS from nanoparticle-associated plasmonic hotspots. Bi et al. [71] introduced digital colloid-enhanced Raman spectroscopy by tuning the concentration of hydroxylamine-reduced silver colloids to 0.5 nM to achieve statistically uniform plasmonic enhancement hotspots throughout the biological sample. By reducing hotspot-to-hotspot variability, this approach improves the effective SNR across the sample, achieving sub-femtomolar detection limits for biochemical populations in solution. Looking towards plasmonic enhancements from nanopatterned substrates, Erkizan et al. [72] designed laser-induced nanoripple structures of varying periodic frequency within Si substrates, subsequently coated with a silver coating to create plasmonic hotspots (Figure 5a). This structure enhanced the Raman signal by up to 10^9-fold, enabling improved SNR through amplification of Raman signals from molecules localized within the plasmonic near field. Utilizing a 100 nm thick column-structured silica layer on the Ag nano island substrate, Minamikawa et al. [73] achieved Raman signal enhancement by 10^7-fold through a remote plasmonic-like enhancement effect, improving the effective SNR for enhanced Raman signals. Some other strategies focus on intrinsic material properties or laser excitation modifications to enhance Raman signals. In a study by Domes et al. [74], signal detection capabilities are enhanced through field enhancements enabled by the use of ultraviolet (UV) light at specific wavelengths resonant with electronic transitions in biomolecules, named as deep ultraviolet resonance

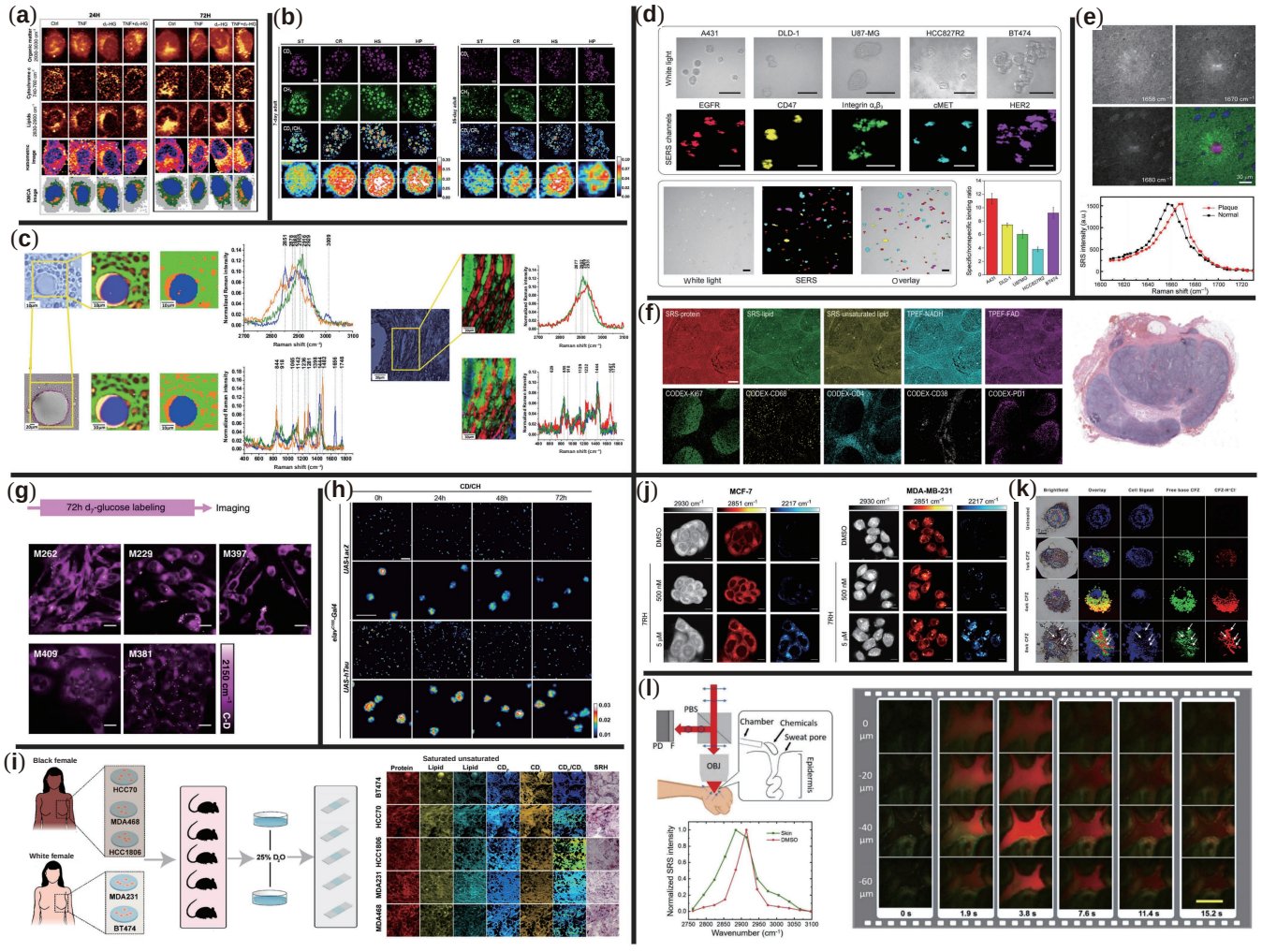


Figure 3 Raman microscopy applications in biomedical imaging of cell, animal, and human tissue for cell metabolism (**a**–**c**), tissue mapping (**d**–**f**), disease progression (**g**–**i**), and pharmacokinetic (**j**–**l**) study. **a.** Cell culture metabolism. Multichannel SRS imaging of HMEC-1 cells under high glucose and TNF-driven inflammation shows time-dependent increases in lipid content and mitochondrial activity [45]. **b.** Animal model metabolism. DO-SRS imaging of Drosophila lipid turnover rates under varied diets, revealing accelerated catabolism under high protein conditions and lipid storage under high sugar conditions [46]. **c.** Human tissue metabolism. Raman imaging of normal vs. breast cancer tissue maps glycans, lipids, and proteins, clarifying metabolic changes linked to tumor infiltration [49]. **d.** Cell culture mapping. SERS Tagged imaging detects and maps the spatial distribution of cocultured cell lines, achieving multiplexed molecular profiling of cancer cells [51]. **e.** Animal model tissue mapping. SRS imaging of amyloid plaques in brain tissue samples from an Alzheimer's disease mouse model. Three-color SRS images identify the spatial distribution of lipids (green), normal protein (blue), and amyloid plaque (magenta) [54]. **f.** Human tissue mapping. SRS imaging combined with high-plex immunofluorescence (REDCAT) enables submicron mapping of cell composition and metabolism across entire lymph node sections [56]. **g.** Cell culture disease progression. SRS imaging of deuterated glucose in melanoma lines reveals higher fatty acid synthesis in more differentiated cells [57]. **h.** Animal model disease progression. DO-SRS imaging of Drosophila expressing human Tau protein highlights lipid dysregulation, unsaturated lipid buildup, and enlarged lipid droplets [58]. **i.** Human tissue disease progression. SRS imaging of triple negative breast cancer (TNBC) subtypes from African American and Caucasian origins distinguishes variations in metabolic activities and biomolecular composition, particularly lipid unsaturation ratios, de novo protein & lipid synthesis, and cytochrome C distribution [60]. **j.** Cell culture pharmacokinetics. Live-cell SRS imaging of DDR1 inhibitor 7RH tracks drug uptake via protein, lipid, and alkyne channels, showing dose-dependent accumulation [64]. **k.** Animal model pharmacokinetics. Imaging clofazimine (CFZ) drug accumulation within alveolar macrophages extracted from mouse lungs. Through Raman imaging, distinct cellular components are differentiated from spectral signatures associated with protonated and deprotonated forms of CFZ, enabling drug accumulation tracking across an 8-week timespan [65]. **l.** Human tissue pharmacokinetics. Two-color SRS volumetric imaging tracks DMSO penetration in human sweat pores via skin (2,884 cm^{-1}) and DMSO (2,914 cm^{-1}) peaks [68].

Raman spectroscopy. Resonance enhancement selectively amplifies target vibrational modes, increasing their signal relative to broadband background, thus effectively improving SNR. Liang et al. [75] developed ionic-wind-enhanced Raman spectroscopy to detect fluorescent and vulnerable samples without a substrate. Using ionic wind generated by a needle-net electrode to induce charge transfer and local field effects, the Raman response was enhanced. Incorporated with photobleaching to suppress fluorescent background, this technique increased the SNR of Raman signals by 3-fold compared to photobleaching alone.

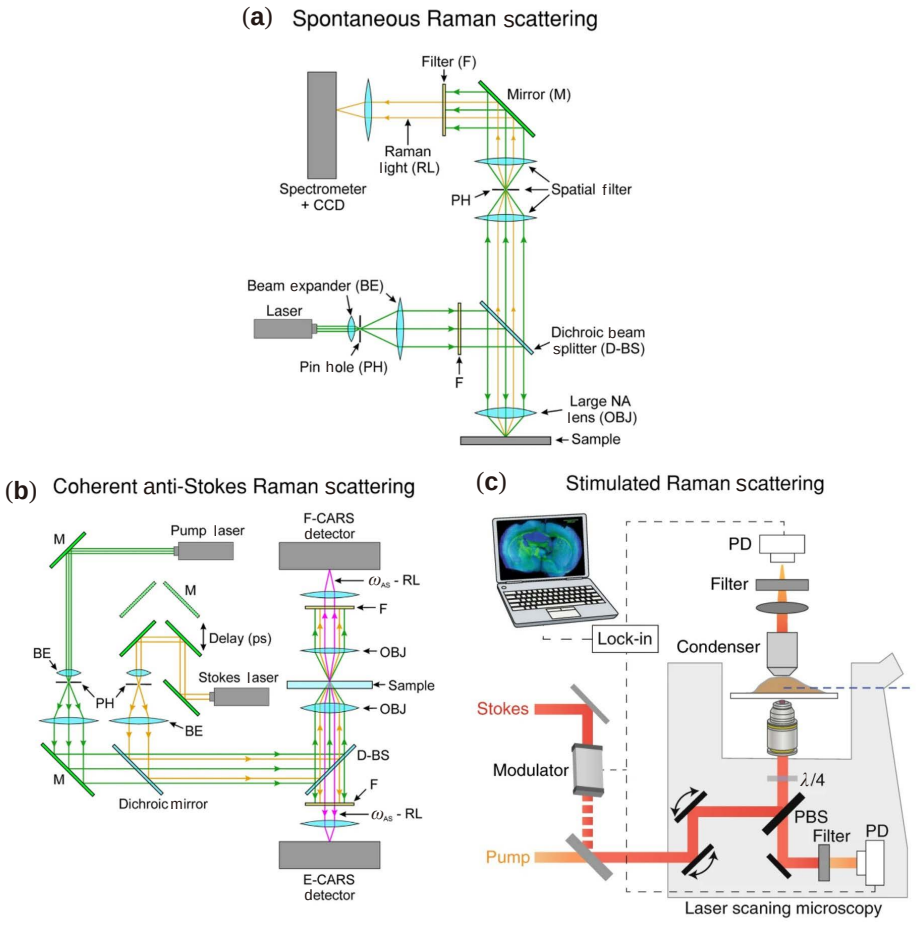


Figure 4 Characteristic schema of Raman microscopy modalities. **a.** Spontaneous Raman scattering microscopy. In confocal spontaneous Raman microscopy, an exciting pump beam is spatially filtered through a pinhole while backscattered light is additionally spatially and spectrally filtered through a notch filter. Raman scattered photons are analyzed through the combination of a spectrometer and charge-coupled device, enabling hyperspectral images to be acquired as the focal point is raster scanned across the sample [5]. **b.** CARS microscopy. In confocal CARS microscopy, two laser sources provide the Stokes and pump beams that are synchronized through a specialized picosecond path difference mirror scheme. Incident light is focused on an optically transmissive sample substrate for signal acquisition from forward and backward scattered light. Forward scattered light (F-CARS) and backward (or epi) scattered light (E-CARS) are filtered through bandpass filters and detected by dedicated avalanche photodiodes. Images are obtained by raster scanning the focal point across a sample of interest while hyperspectral acquisition is enabled through laser energy tuning [5]. **c.** SRS microscopy. In confocal SRS microscopy, two laser sources provide synchronized Stokes and pump beams. Additionally, high-frequency modulation is applied to the Stokes beam for suppression of low-frequency laser intensity fluctuation noise through the utilization of a lock-in amplifier set to the modulation frequency. Raman signals can be measured from intensity fluctuations from Stokes light in transmission and reflection configurations, focused on an optically transmissive sample substrate and directed to a photodiode. Images are obtained by raster scanning the focal point across a sample of interest while hyperspectral acquisition is enabled through laser energy tuning [69].

4.1.3 Improving Raman imaging speed

Techniques to enhance the speed of spontaneous Raman imaging take on a wide array of forms with a primary focus on reducing pixel dwell time through spectral compression, spatial parallelization, and signal amplification. Widefield illumination schemes enable parallel acquisition across pixels in Raman imaging that dramatically improve imaging speed. Using a wide-field Fourier-transform hyperspectral Raman microscope, Ardini et al. [76] achieved simultaneous collection of Raman spectra across ~250,000 pixel. This is achieved by integrating a uniform illumination scheme with interferometric detection, which removes the need for point-by-point raster scanning, enabling dwell time an order of magnitude lower in comparison to standard Raman techniques. Wang et al. [77] reported a high-throughput super-resolution Raman imaging approach. By engineering a spatially varying profile of illumination for wide parallelization, they achieved a spatial resolution of 80 nm and imaging time within seconds for a 32 μm × 32 μm field of view. Compressive Raman approaches increase imaging speed bottlenecked by hyperspectral acquisition by compressing Raman spectra acquired at each pixel, enabling increased imaging speeds by reducing the number of spectral measurements required per pixel while preserving chemically relevant information. By implementing near-infrared compressive Raman imaging with a digital micromirror device (DMD) and a single pixel detector, Grand et al. [78] achieved imaging of a mixture of 5 species (2 polymorphs and 3 excipients of drugs) with a pixel dwell time as low as 2.5 ms (Figure 5b). In a similar study, Sturm et al. [79]

optimized a spectral encoding DMD to balance speed with spectral resolution upon reconstruction from spectrally filtered signals, and achieved a speed twice as fast as conventional spontaneous Raman imaging. In a recent notable modification to light sheet microscopy approaches, Guo et al. [80] were able to achieve full-frame hyperspectral imaging within seconds to minutes using a tiled light sheet illumination approach that extended the simultaneously illuminated region of the sample as opposed to sequential probing of individual planes.

4.1.4 Volumetric imaging capability

Recent efforts to enhance the volumetric imaging capabilities of spontaneous Raman microscopy include computational reconstruction of z-stacks, spectral tomographic integrations that recover depth from projection data, and polarization-sensitive spectroscopic techniques that encode axial information. Several studies have employed spectral unmixing algorithms to maximize the utility of z-stack images acquired from existing confocal spontaneous Raman microscopy schemes, which are commonly limited by signal strength and optical sectioning constraints in direct volumetric imaging. Processing hyperspectral z-stacks with vertex component analysis, Kallepitis et al. [81] unmixed biomolecular signatures to reconstruct subcellular features in stem and immune cells. Similarly, LaLone et al. [82] mapped biomolecular population distributions in 3D liver organoids at subcellular resolution by using spectral unmixing algorithms associated with quantitative chemometric phenotyping approaches. Integrating optical projection tomography with Raman imaging, Wang et al. [83] obtained 3D structural and molecular imaging of large biological samples by reconstructing images collected from multiple angles, recovering volumetric information from projection measurements rather than direct depth scanning through the use of filtered back-projection algorithms. A later work by Stepula et al. [84] employed Raman Spectral Projection Tomography to reconstruct 3D molecular maps of live tissue samples from full 2D Raman projection datasets (Figure 5c). Another approach to enhancing volumetric imaging relies on the reconstruction of volumetric maps from the sensitivity of Raman vibrational signatures to polarization states, where pharmaceutical tablets are 3D imaged with 1.7 μm axial resolutions through the sequential acquisition of Raman signals from 9 distinct polarization state scans. This allows axial structure to be inferred from polarization-dependent signal variations as opposed to direct physical optical sectioning [85].

4.1.5 Enhancing spatial resolution

Techniques to enhance the spatial resolution of spontaneous Raman focus on localized electromagnetic field confinement and plasmonic localization-based strategies. These strategies bypass the diffraction limit by restricting the effective Raman excitation volume. Enhancing the spatial resolution through a nanoparticle library of 26 distinct Raman reporters, Eremina et al. [51] obtained precise biomarker distribution imaging with subcellular resolution (~250 nm), beyond the conventional confocal limits. This was achieved by spatially localizing spectrally distinct Raman reporters to discrete nanoparticle sites. Mrđenović et al. [86] used the extremely localized near-field enhancement from silver nanoparticle coating an atomic force microscopy tip (tip-enhanced Raman spectroscopy (TERS)), confining Raman excitation to a few-nanometer interaction volume, to map biochemical species in pancreatic cell membranes with a 2.5 nm spatial resolution (Figure 5d). Another paradigm harnesses stochastic intensity fluctuations from gold nanostars to enable super-resolved Raman imaging through signal localization at sites of nanoparticle-membrane receptor interactions in colon cancer cells [87]. Exploring the potential for nanoparticle array structures to further confine electromagnetic fields, Lee et al. [88] engineered gold nanoparticle arrays hosting localized surface plasmon hotspots that confined the effective Raman excitation volume, enabling a 4-fold increase in lateral resolution. Liebel et al. [89] utilized an interferometric detection scheme to simultaneously record the phase and amplitude of wide-field Raman images. Pairing phase-resolved reconstruction with plasmonic field enhancements from supercluster nanoparticles enabled sub-diffraction precision in 3D multiplexed Raman imaging.

4.1.6 Summary

A central theme in advances in spontaneous Raman microscopy is to overcome its intrinsic low efficiency while preserving the chemical specificity of the approach. Strategies to enhance the SNR include plasmonic amplification, resonance excitation, and field-enhancing substrates. They enable orders of magnitude improvements in signals but also introduce tradeoffs associated with probe heterogeneity, substrate dependence, increased sample preparation complexity, and biological compatibility. Additionally, approaches to accelerate imaging speed include widefield illumination, compressive sensing, and spectral encoding. These methods reduce pixel dwell time but at the expense of spectral resolution and possibly quantitative accuracy. A common theme emerges that enhancement in SNR or speed is often accompanied by tradeoffs in related categories, as well as with increased experimental and computational complexity.

This theme emerges again when considering advancements focused on enhancing volumetric and super-resolved Raman imaging. Computational reconstruction-focused methods enable volumetric molecular mapping beyond traditional depth limits, but are still hampered by traditional constraints involving signal attenuation, scattering, and reconstruction faithfulness in optically dense tissues. Similarly, spatial resolution enhancements are largely achieved through plasmonic confinement, and near-field techniques can achieve nanometer precision but are limited to surface-accessible tissue regions, specialized substrates, or non-physiological conditions. While spontaneous Raman microscopy is a versatile tool, its utilization should be considered in an application-dependent fashion with serious evaluation of tradeoffs between sensitivity, resolution, imaging speed, photodamage potential, and the ultimate biological goal when designing for optimal performance.

4.2 The limitation of coherent Raman scattering

4.2.1 Challenges and limitations of coherent Raman scattering

A major limitation in CRS microscopy schemes (Figure 4b) is the presence of a non-resonant background due to the four-wave mixing processes within the sample. This directly interferes with

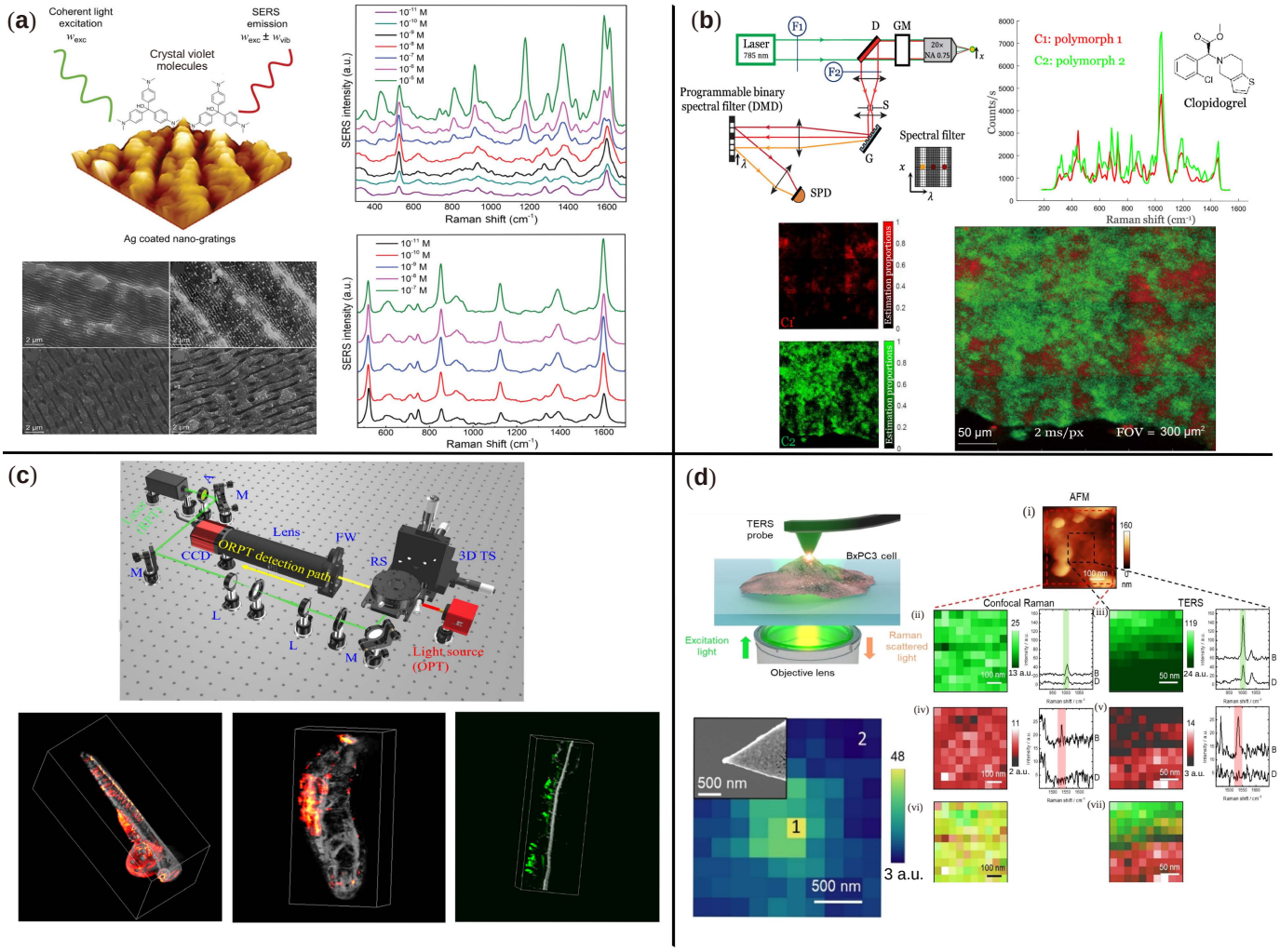


Figure 5 State of the art advancements in spontaneous Raman imaging. **a.** Signal-to-noise ratio. Utilization of Ag-coated laser-induced periodic surface structures to further enhance SERS signals. Dramatic signal-to-noise enhancement in the detection of Crystal violet molecular concentrations down to 10^{-11} M (1 M = 1 mol L^{-1}) [72]. **b.** Imaging speed. Integration of a compressive Raman technology (CRT) setup within a spontaneous Raman microscopy imaging scheme utilizing a DMD for rapid imaging through fast switching between programmed spectral channel filters selectively directed to a single pixel detector. Imaging of the spatial distribution of polymorphs of clopidogrel within pharmaceutical tablets with pixel dwell time of 2.5 ms [78]. **c.** Volumetric imaging. Spontaneous Raman spectroscopy integrated with optical projection tomography to add chemical mapping to microstructural details acquired through the capture of diffuse reflection light at various rotated sample positions. 3D volumetric reconstructions of zebrafish and Drosophila larva imaging with red areas identifying lipid and protein distributions [84]. **d.** Spatial resolution. TERS imaging of BxPC-3 pancreatic cancer cell membrane. Left images show 2-channel conventional confocal Raman imaging of the cell surface with 210 nm resolution and a homogenous appearance, while right images exhibit TERS images achieving 2.5 nm resolution, clearly delineating the cellular membrane boundary [86].

the Raman signal generated, contributing to spectral distortion and making detected signal intensities less vibrational bond specific. A direct consequence of this is an intrinsically lower sensitivity of CARS for the detection of low-concentration analytes than other Raman schemes, as its signal scales quadratically with molecular concentrations. Interference between non-resonant background processes and Raman signals also makes spectral data less dependable, which requires complex phase retrieval methods such as Kramers-Kronig relations to reconstruct unpolluted Raman spectra. Another limitation of CARS is the bottleneck placed on spectral acquisition by the need to individually tune the pump and Stokes beams to target vibrational bond energies in generating a full spectrum. This challenge is further compounded by spectral distortions from non-resonant background processes, degrading the spectral resolution. Additionally, unlike spontaneous Raman, the spectral resolution in CRS microscopy is intrinsically coupled to excitation bandwidth, pulse duration, and acquisition strategy, making it more of a considered constraint [90].

Challenges with SRS microscopy schemes (Figure 4c) stem from its alternative paradigm for signal detection through intensity fluctuations. As the detection of vibrational mode signatures depends on the magnitude of intensity fluctuations in either the pump or Stokes beam, SRS requires high-frequency modulation together with a lock-in amplifier detection to read out signals. These fractional intensity changes are small enough to also be susceptible to laser intensity fluctuations, requiring stringent standards on laser stability and noise suppression techniques to

maintain high SNR. Like CARS, SRS faces a limit to the speed of hyperspectral image acquisition owing to the same bottleneck generated by the need to sweep laser energies to coherently drive vibrational modes. However, more recent advancements (reviewed below), such as the Fourier transform and spectral focusing approaches, have now proven the capability of fast multiband acquisition. Additionally, since SRS detects modulation synchronous intensity changes, the approach is largely immune to interference effects from phenomena like autofluorescence within samples. SRS has clear benefits as a Raman-based microscopy approach compared to direct photon-based detection in CARS and spontaneous Raman microscopies. While both modalities face technical constraints, the absence of a non-resonant background in SRS provides a clear advantage for quantitative bioimaging, motivating its adoption as the primary coherent Raman modality emphasized in the following sections reviewing advances addressing the limitations of CRS-based microscopy [91] (Figure 6).

4.2.2 Enhancing the signal-to-noise ratio of CRS

Enhancing the SNR in CRS microscopy is closely coupled to strategies that improve spectral discrimination, temporal encoding, or detection specificity rather than direct signal amplification alone. Many SNR enhancement approaches achieve signal discrimination by improving effective sensitivity through separation of resonant Raman responses from non-resonant background or laser noise through time-domain, frequency-domain, or modality-specific detection schemes. Early demonstrations of SNR improvement were first developed in CARS microscopy, including Fourier-transform CARS, Matrix Pencil modeling, spatial-frequency encoded line scanning, electronic-resonance CARS, and hyper-Raman scattering extensions. These methods have advanced SNR through enhancements to either spectral resolution or signal amplification, though non-resonant background remained a limiting factor [92-96]. Similar to CARS microscopy, spectral resolution enhancements in SRS focus on techniques to increase SNR through time domain approaches as well as alternative detection and excitation schemes. Lin et al. [97] acquired SRS spectra at 10 cm^{-1} spectral resolution within 20 μs by integrating a polygon scanner with a Littrow-configured reflective grating, which temporally delayed frequency components from a broadband excitation source. With electronic preresonance in the visible wavelength regime, Zhuge et al. [98] significantly boosted the imaging sensitivity to 34 micromolar with a dwell time of 10 μs, and achieved a spectral resolution of 10 cm^{-1}. Another approach adapts the benefits achieved from FT-CARS for SRS by encoding time domain response within SRL signal using a femtosecond pulse–pair sequence, through which Yu et al. [99] achieved natural linewidth limit for spectral resolution (~−5–10 cm^{-1}). Xiong et al. [100] employed SRS to coherently excite a vibrational mode and subsequently upconvert the excited state to a fluorescent state with an additional pump beam for fluorescent emission. Through additional SNR enhancement from preresonant excitation, single-molecule Raman detection was achieved. To enhance SNR in SRS microscopy, Zhu et al. [101] developed stimulated Raman photothermal (SRP) microscopy that changes the paradigm of detecting SRS signal from intensity variations to the index of refraction changes from the energy dissipation resulting from coherent vibrational excitation. Detecting these changes through refraction of an idle continuous wave laser, the technique achieves a 500-fold boost in modulation depth relative to conventional SRS, enabling ultrahigh sensitivity imaging down to micromolar concentrations (Figure 6a).

4.2.3 Improving imaging speed

Strategies to increase imaging speed were also pioneered in CARS, where parallelization, plasmonic enhancement, dual-frequency combs, and rapid Stokes modulation enabled faster acquisition and reduced dwell times [102-106]. Imaging speed improvements in SRS microscopy include optimizing laser sources, parallelization methods, and spectral scanning improvements. Due to the nature of SRS detection being focused on fractional intensity fluctuations, laser stability improvements often directly translate into many improvements to competencies related to bioimaging, including speed. Integrating a two-color pulsed fiber laser, Kong et al. [107] used cross-phase modulation of the fiber to passively generate synchronized pump and Stokes pulses, reducing noise by ~50 dB, and achieving a pixel dwell time of 6.4 μs. Parallelization strategies have emerged that enhance speed through simultaneous multiplex imaging. In an approach named collinear multiple beam SRS, Li et al. [108] achieved multiplex imaging by integrating two acousto-optic deflectors to split the pump and Stokes beams into 46 simultaneous foci (or channels) and obtained an imaging speed of 2,000 frames per second with a pixel dwell time of 7 μs, which enabled real-time tracking of polymerization dynamics. Efforts have also targeted the enhancement of spectral acquisition speed for hyperspectral imaging. Incorporating a spatial light modulator (SLM) into traditional SRS microscopy, Bae et al. [109] replaced the traditional laser tuning scheme with dynamic sparse sampling masks, which selectively filtered Raman excitation bands from a broadband excitation source, and obtained rapid multichannel imaging with a 2.4 μs pixel dwell time and frame rate of 70 ms (Figure 6b). In another approach, Ni et al. [110] developed a SRS microscopy by using rapidly tunable fiber optical parametric oscillators that achieved wavelength tuning in just 5 ms, which dramatically improved the spectral acquisition speed.

4.2.4 Volumetric imaging capability

In CRS microscopy, volumetric imaging is fundamentally constrained by the need for sequential axial scanning, limited penetration depth due to scattering, and the tight coupling between excitation geometry and depth discrimination. Enhancing volumetric imaging in coherent Raman microscopy has centered on overcoming the intrinsic depth and speed limitations of point-scanning approaches, with strategies ranging from widefield excitation and advanced reconstruction methods to hardware innovations and optical clearing. CARS innovations toward volumetric imaging have included widefield speckle illumination, hyperspectral 3D reconstruction, achromatic metalenses, and polarization-resolved molecular orientation mapping, each broadening volumetric capability in distinct ways [111-114]. Efforts to improve volumetric imaging capabilities in SRS microscopy include finding alternatives to mechanically based z-scanning and approaches for greater penetration depth. In a

technique named SRS tomography, Gong et al. [115] achieved z-scan-free volumetric imaging by using diffraction-free Bessel beams in conjunction with a SLM to generate an optical beating pattern that encodes depth information in the spatial frequency domain. Retrievable by Fourier transform, the technique achieves a 2x increase in imaging depth over conventional SRS microscopy. Utilizing ultraslow Bessel beam pulses to encode depth information in the time domain, Lin et al. [116] introduced Bessel light bullet-enabled time-of-flight SRS to replace mechanical z-scanning with relative time-of-flight detection, and reached a 2x increase in penetration depth in porcine brain tissue (Figure 6c). Another approach enhanced volumetric SRS imaging by dynamically adjusting the wavefront through a deformable mirror, instead of moving the objective lens, for depth mapping that eliminated aberrations and realized an axial scan range of ~41 μm. [68]) In addition to hardware improvements, strategies have also been taken towards sample treatment and laser source. Wei et al. [117] introduced a tissue clearing technique that used urea solution to reduce light scattering by homogenizing the index of refraction profiles, which increased the imaging depth to 1 mm in brain tissue. Moester et al. [118] employed an optical parametric oscillator to generate pump-Stokes pairs at wavelengths greater than 1,500 nm, which naturally reduced the scattering and achieved 2x deeper penetration compared to conventional SRS.

4.2.5 Enhancing spatial resolution

Efforts to enhance spatial resolution in coherent Raman microscopy have explored nonlinear excitation schemes, interferometric detection, plasmonic confinement, depletion-based approaches, and tailored probes, all aiming to push beyond the diffraction limit. CARS microscopy has a history of pushing spatial resolution through higher-order nonlinear processes, phase-sensitive interferometry, plasmonic nano-focusing, and TERS integration, achieving super-resolution in specialized implementations [119-123]. A variety of approaches have also been taken to improve the spatial resolution of SRS microscopy, including the utilization of shorter wavelengths, depletion-based techniques, sample treatments, and contrast enhancement approaches. Realizing the theoretical enhancements to spatial resolution and sensitivity afforded by SRS driven by shorter wavelengths of light, Lin et al. [124] developed ultrasensitive reweighted visible stimulated Raman scattering (URV-SRS) integrating chirped pulse excitation along with a noise suppression algorithm to resolve photodamage and non-Raman background noise from visible light-driven SRS, respectively. This development increased detection sensitivity by a factor of ~50 at a lateral resolution of 86 nm and axial resolution of 400 nm, respectively. Utilizing saturation effects to improve spatial resolution in SRS microscopy, Gong et al. [125] developed saturated SRS microscopy that sharpens point spread functions by suppressing Raman-active molecules at the edges of the focal point through nonlinear saturation. Coupling this approach with a virtual sinusoidal modulation method to account for signal changes associated with increased intensity, they obtained a 1.48x enhancement in lateral imaging resolution. Integrating stimulated emission depletion (STED) with the previously mentioned stimulated Raman excited fluorescence (SREF), Xiong et al. [126] achieved a 2x enhancement in spatial resolution by using a donut-shaped STED depletion beam to minimize the effective fluorescent excitation volume. More recently, Shou et al. [127] introduced a reversible saturable optical Raman transitions (RESORT) microscopy, which combined photoswitchable Raman tags with STED-based point spread function, and achieved two-fold improvements in spatial resolution along with high contrast (Figure 6d). Sample treatment and Raman tags have also been developed to improve imaging resolution. Using a technique named Molecule Anchorable Gel-enabled Nanoscale Imaging of SRS, Shi et al. [128] achieved lateral resolutions of ~41 nm by using a hydrogel matrix to uniformly expand biological samples for imaging. Alternatively, Ao et al. [129] engineered photoswitchable probes to enable the selective activation of specific vibrational modes, allowing for improved super-resolution imaging with high contrast.

4.2.6 Summary

Advances in CRS microscopy highlight a sustained effort to balance sensitivity, spectral fidelity, and imaging speed from the constraints resulting from nonlinear excitation and detection. In particular, CARS offers strong signal levels through coherent signal generation, but its susceptibility to non-resonant background fundamentally limits signal specificity, and quantitative interpretation requires complex phase retrieval tools or spectral reconstruction strategies. In comparison, SRS eliminates non-resonant background, which enables direct linear concentration scaling, making it ideal for quantitative biomedical imaging despite increased requirements on laser stability, modulation schemes, and noise suppression.

The advancements in enhancing CRS microscopy performance in SNR, volumetric imaging, and spatial resolution illustrate the tradeoffs that manifest when designing solutions to resolve specific limits associated with coherent excitation schema. Time-domain encoding, spectral focusing, and alternative detection paradigms improve effective sensitivity and spectral resolution but naturally introduce additional hardware complexity and computational demands. As described above, innovations achieving benchmarks in volumetric and super-resolved CRS imaging have exceeded conventional limits through approaches like wavefront shaping, nonlinear saturation, and probe engineering. However, many of these still face limits in scattering, penetration depth, and most importantly, proving biological compatibility in more generalized conditions. Once again, the selection of CRS microscopy configuration is largely dependent on the specific biological question of interest. As time progresses, many individual enhancements to imaging speed, SNR, volumetric imaging, and spatial resolution will likely become more integrated in nature, relaxing current tradeoff decisions.

5. Software development in image processing

With the ability of Raman microscopy to collect multiplexed data across spectral channels and depth profiles at increasing resolutions, techniques to extract all salient information from these rich data sets are imperative. In CRS microscopy, software-based image processing is particularly important, as computational methods are required to push past fundamental limits in data acquisition,

stemming from laser intensity noise, spectral mixing, and tradeoffs between spectral resolution, sensitivity, and imaging speed.

Software development in CRS image processing has evolved to address functional challenges within the Raman imaging pipeline, including noise suppression, spectral unmixing, feature extraction, and data-driven classification in biological and translational contexts. Machine learning algorithms offer opportunities in this regard with their inherent focus on identifying key patterns in data sets through statistical analysis. Regarding Raman microscopy applications in bioimaging, software implementations to data analysis generally revolve around efforts to increase the spectral and spatial resolution of images, translational medicine applications in biological feature identification and histology, and improvements to identifying biochemical species (Figure 7) [130]. Accordingly, this section is organized to reflect software-based enhancements to the CRS image-analysis pipeline, with Sect. 5.1 focusing on software methods that enhance the resolvable signal and resolution of images, Sect. 5.2 addressing biological feature

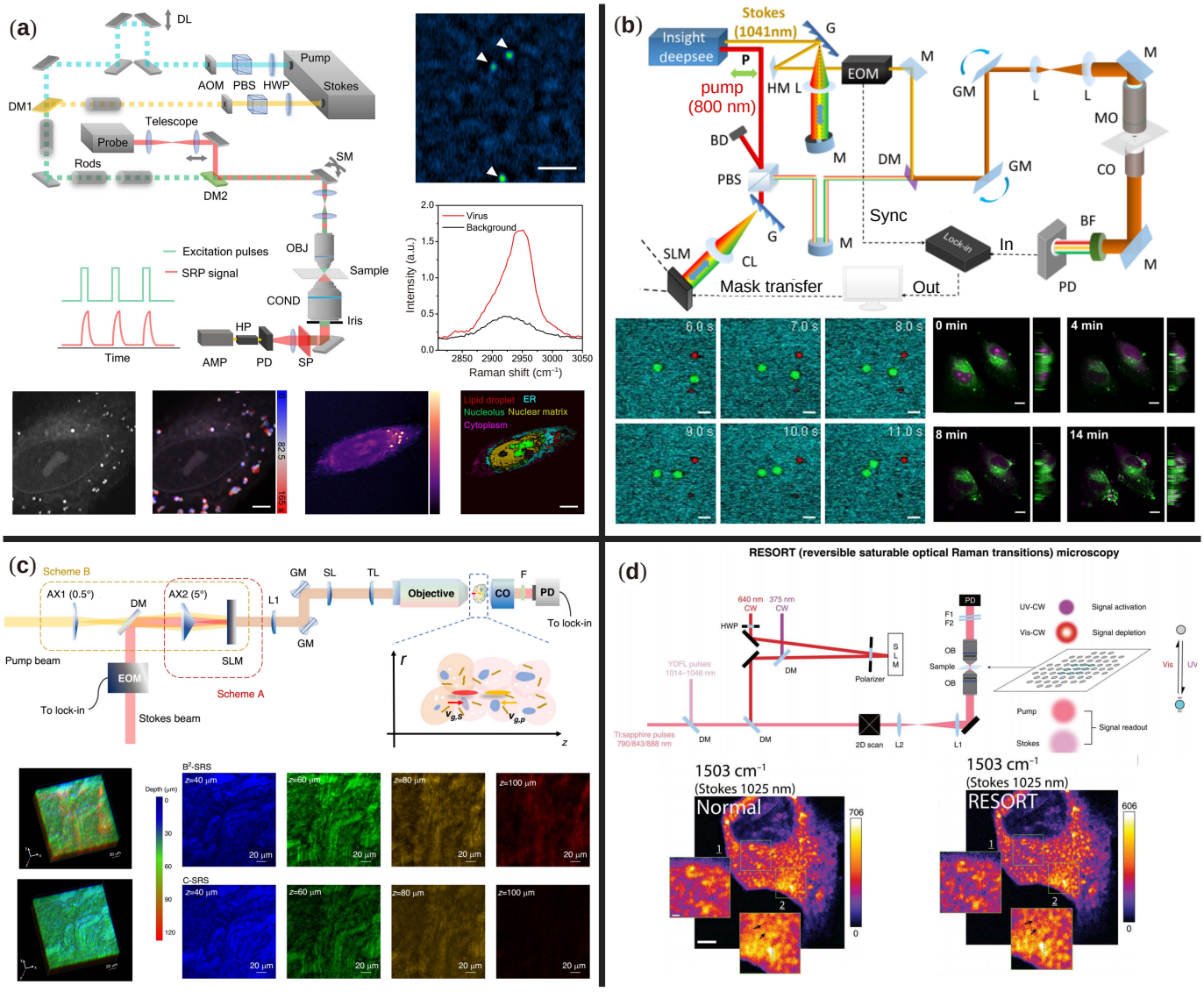


Figure 6 State of the art advancements in stimulated Raman imaging. **a.** Signal-to-noise ratio. SRP microscopy utilizes the photothermal effect induced by the vibrational relaxation of Raman-excited molecules, detecting changes in refractive index from localized heating as opposed to gain/loss in the Stokes or Pump beam. SRP enables a 21.2-fold improvement in SNR, allowing for clearer imaging of cellular structures and even imaging of individual varicella-zoster virus [101]. **b.** Imaging speed. SLM-SRS integrates an SLM that utilizes sparse sampling masks to selectively excite spectral windows with rapid mask-switching. This enables multiplexed live cell imaging within 3 seconds per frame of HeLa cells under alkaline stress [109]. **c.** Volumetric imaging. B^2-SRS utilizes counterpropagating Bessel light bullets traveling at ultraslow group velocities for enhanced optical sectioning. The Bessel light bullets are generated by angular dispersion control through integrating an SLM and axicons with an SRS signal generated at tissue depths where the counter-propagating pump and Stokes beams overlap spatially and temporally. 120 um depth resolved B^2-SRS imaging of porcine brain tissue samples compared to conventional SRS depth resolution of 80 um [116]. **d.** Spatial resolution. RESORT microscopy uses two continuous wave lasers at different wavelengths to selectively activate and deactivate the Raman signal for precise control of which molecules are Raman active under a traditional SRS microscopy imaging scheme. Through selective switching of vibrational transitions by donut-shaped depletion beams, the point spread function is sharpened, achieving a spatial resolution of ~150 nm in imaging fixed (top) and live (bottom) HeLa cells in comparison to traditional SRS imaging (left) [127].

detection and histological interpretation, and Sect. 5.3 reviewing approaches for biochemical classification through analysis of hyperspectral image data.

5.1 Enhancing spectral and spatial resolution

Computational approaches for enhancing spectral and spatial resolution in CRS microscopy can be broadly categorized into two classes. First, super-resolution image reconstruction. High-resolution images can be effectively inferred from undersampled or lower-resolution images. Second, spectral denoising and artifact suppression techniques. These techniques improve the spectral resolution in hyperspectral data sets by limiting the effects of noise, baseline distortions, and non-resonant background contributions that obscure image quality.

Deep learning-based super-resolution techniques can reconstruct high-resolution Raman images from lower-resolution or high-speed acquisitions. Haque et al. [131] applied a residual network-based convolutional neural network (CNN), trained on 54 paired low- and high-resolution Raman images, to reconstruct high-resolution Raman images from low-resolution input and increased the spatial resolution by 4-fold. Similarly, He et al. [132] utilized a CNN to transform low-resolution images captured from high-speed line scan conditions to high-resolution images, enabling a 5-fold reduction in imaging time while maintaining high spatial resolution. Beyond learning based approaches, Jang et al. [133] developed an adaptive pointillism-based deconvolution (A-PoD) algorithm, which reconstructed images through the optimization of a fixed number of virtual emitters to a point spread function, and obtained an enhanced spatial resolution below 59 nm (Figure 7a).

In parallel, classical and learning-based computational denoising and artifact-suppression approaches improve effective spectral resolution by correcting instrument-associated noise, baseline distortions, and non-resonant background contributions. Along with learning-based methods, classical signal processing techniques such as Savitsky-Golay filtering, polynomial baseline correction, and multivariate methods like principal component analysis (PCA) and multivariate curve resolution (MCR) represent widely used tools for suppressing noise and improving spectral clarity in Raman imaging data. Building on this foundation, He et al. [134] developed a noise learning approach to remove optical instrument-associated noise from hyperspectral Raman data by training a deep learning model on spatial frequency noise patterns across a pixelated field of view, improving the SNR by 10-fold and sharpening the Raman spectra collected. Using a generative adversarial network to generate 10,000 simulated Raman spectra from Gaussian noise, Hu et al. [135] trained a CNN for spectral denoising and baseline correction, reducing root mean square error within Raman images by 88%. Similarly, Velensise et al. [136] applied CNNs to CARS microscopy data to suppress non-resonant background artifacts, improving spectral clarity without modifications to Raman imaging hardware.

5.2 Biological feature detection and histology

Another application field of machine learning in biomedical Raman imaging is its potential in cell feature detection and histopathology in near real-time in the clinical setting. For Raman-based biological feature detection, Zhang et al. [137] employed a deep learning-based cell counting algorithm, trained on high-resolution SRS images of H&E-stained brain tumor tissues, to automate cancer cell identification and achieved an R-value of 0.97 relative to H&E cell counts. More recently, Lu et al. [138] developed an approach that restructured Raman spectra into image-like 2D signal aggregated representations for better spectroscopic deep learning. When tested on benchmark Raman datasets, neural networks trained on this data exhibited improved classification accuracy by 2%–4% over state-of-the-art approaches with 85%–97% accuracy in identifying a variety of cell phenotypes. In the realm of histopathology, a number of computational implementations aim to match or exceed the diagnostic capabilities of H&E staining. Integrating deep learning models into femtosecond stimulated Raman histology (SRH), Liu et al. [139] utilized a U-Net deep learning model, trained on over 100 fields of view of HeLa cells and gastric specimens, to classify cancerous cells with a diagnostic accuracy of >96%. Hollon et al. [140] combined SRH and a deep CNN, which was trained on over 2.5 million SRH images from 415 patients, for intraoperative diagnosis of brain tumors and obtained noninferior accuracy compared to conventional histology. Additionally, integrating semantic segmentation approaches into the model allowed for precise tumor margin identification to guide surgery in under 3 min. Building on this clinically validated framework, Kondepudi et al. [141] extended this paradigm, using large-scale foundational models pretrained on Raman and histological data, to achieve label-free tumor detection with improved generalization and reduced dependence on task-specific retraining steps. Liu et al. [142] developed a semi-supervised CycleGAN architecture to virtually stain SRS images of fresh brain tumor tissues using unpaired training, and achieved higher diagnostic accuracy of brain tumor compared with conventional H&E staining (Figure 7b). This approach is promising for intraoperative diagnosis of brain tumors in near real time.

5.3 Biochemical classification

Machine learning-based biochemical classification in CRS microscopy focuses on resolving biochemical subpopulations exhibiting spectral overlap in hyperspectral imaging data. In supervised learning scenarios, neural networks have been trained directly on Raman spectra to discriminate biochemical features within Raman spectra. Using a 1D CNN model trained on Raman spectral datasets of a variety of viral species, Ye et al. [143] achieved an over 95% accuracy in distinguishing individual viral species from each other, along with the capability to map key Raman peaks to biomolecular structures in samples. In a similar work, Parlatan et al. [144] integrated Raman imaging with an artificial neural network trained on Raman spectra of exosomes from five different cell lines, and achieved a 96.8% classification accuracy in identifying cancer-derived exosomes.

Aside from fully supervised classification strategies, many emerging approaches also set out to disentangle overlapping biochemical contributions using reduced or indirect supervision. Whereas classical spectral unmixing protocols decompose Raman

signals by referencing pure spectra of isolated components, more recent self-supervised approaches use data-driven synthetic representations to improve biochemical characterization without the need for building an extended labeling dataset. For example, using a self-supervised learning model with non-negative autoencoders trained on synthetic and experimental Raman spectra of biomolecular species, Georgiev et al. [145] improved quantitative characterization of individual biochemical species compared to traditional unmixing methods. Complementary to representation learning, similarity-based and reference-matching frameworks remain widely used for biochemical identification in CRS microscopy. Zhang et al. [146] developed a penalized reference matching (PRM) algorithm and applied it to SRS microscopy (PRM-SRS). By adding a penalty term and quantifying the spectral similarities between experimental spectra and reference spectra in the library, this approach achieved enhanced chemical specificity and fast data processing (Figure 7c). Different lipid subtypes in a variety of organs and species were successfully identified. Ju et al. [147] employed a Characteristic Peak Similarity (CaPSim) machine learning algorithm to directly match experimental SERS spectra with Raman spectral libraries. Using similarity-based recognition, the approach corrects for substrate-dependent spectral variations, outperforming existing similarity metrics. Altogether, these approaches highlight a trend in the evolution from explicit spectral matching toward learning-enabled and self-supervised frameworks in CRS-based classification goals.

5.4 Summary

Software-based image processing has become a staple within modern Raman imaging workflows, where computational

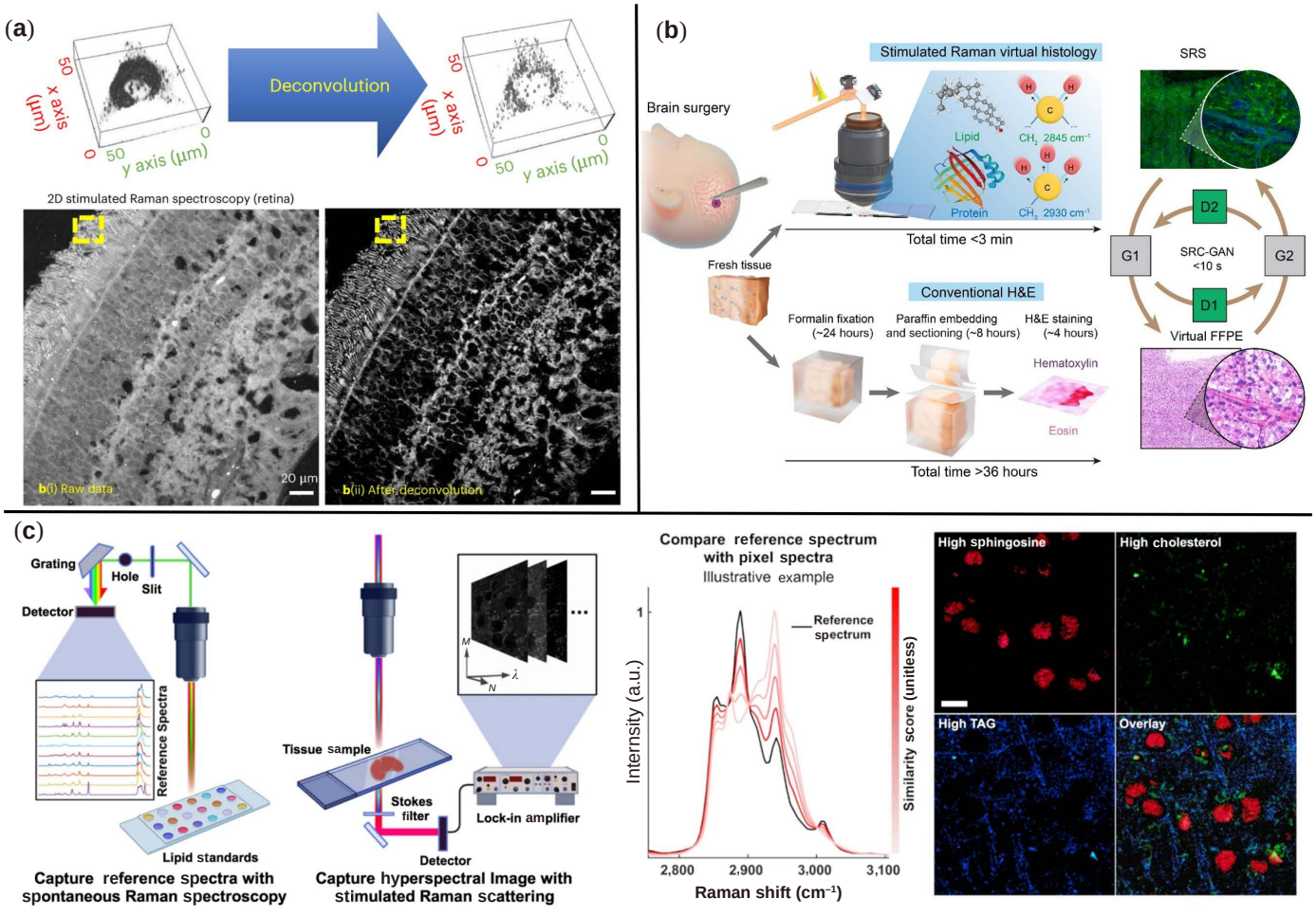


Figure 7 Machine learning based Raman microscopy enhancements in super-resolution, biological feature detection, and biochemical classification. **a.** Scheme for adaptive pointillism-based deconvolution (A-PoD) algorithm achieving super-resolved SRS images through post-processing. Through adaptation of virtual emitters to a point spread function of diffraction-induced blurring from raw SRS imaging data, the approach achieves a spatial resolution of under 59 nm in imaging retinal tissue samples [133]. **b.** Schematic for stimulated Raman virtual histology (SRVH) achieving extremely rapid virtual staining within 3 min with high diagnostic accuracy comparable to traditional H&E-stained tissue images requiring over 36 h of preparation time. Two-channel SRS images of lipid and protein contrasts within samples are processed using a stimulated Raman CycleGAN (SRC-GAN) model, converting these contrasts into virtual formalin-fixed and paraffin-embedded (FFPE)-style H&E stains [142]. **c.** Schematic for lipid subtype identification through PRM SRS. The approach utilizes pure lipid standards to generate spontaneous Raman spectra as a reference standard through a PRM correction algorithm accounting for spectral baseline shifts along with spectral similarity with collected hyperspectral SRS data [146].

techniques are regularly employed to surpass fundamental limitations in signal acquisition, spectral resolution, and noise suppression. Classical signal processing and chemometric techniques remain essential for improving spectral clarity, suppressing artifacts, and enabling quantitative analysis, whereas learning-based approaches have introduced the ability to reconstruct high-resolution images, accelerate acquisition, and extract biologically meaningful features from high-dimensional data. As time progresses, software tools have moved from an auxiliary tool to an essential component in biomedical Raman imaging, meaningfully expanding the limits of effective resolution, sensitivity, and general interpretability of Raman measurements.

While the contributions of software-driven enhancements are clear, it is important to clarify important trade-offs and practical considerations in their utilization. Deep learning models can achieve performance gains but often rely on large, well-curated training datasets that can have limited generalization across instruments, sample preparations, or biological scenarios. Some key open challenges to machine learning-based tools include sensitivity to physical domain shifts and obstacles in validation, especially for translational and clinical applications. It is important to balance performance gains against interpretability and experimental context when selecting computational tools for pre- and post-processing. Continued progress will depend on the integration of physics-informed models with data-driven approaches, the establishment of standardized validation benchmarks, and the development of more generalizable computational workflows that withstand biological and instrumental variability.

6. Emerging technologies

Beyond the directions of technological development featured so far, a number of developing areas of interest are highlighted. These research fields aim to push either the translational potential of Raman-based imaging frameworks or extend current capabilities to delineate biological phenomena further.

6.1 Miniaturization

Recent efforts seek to improve the translational capabilities of Raman imaging modalities by compartmentalizing traditional schema to avoid the bulky experimental schemes these techniques rely on. Using a lab-on-a-chip paradigm to miniaturize Raman characterization, Lin et al. [148] achieved real-time bacterial diagnostics of antibiotic drug efficacy by integrating a microfluidic-based antimicrobial susceptibility testing platform with Raman spectroscopy across 66 individual microwells. Fiber optic-based Raman imaging platforms were developed to expand capabilities for *in vivo* imaging. Žuvela et al. [149] employed a 1.9 m long, 1.8 mm diameter fiber optic Raman probe in endoscopic examinations to capture Raman spectra in the fingerprint region. Through a machine learning algorithm trained on over 2,000 Raman spectra, the probe achieved >98% accuracy in cancer diagnosis. Similarly, Plesia et al. [150] created a fiber optic probe for *in vivo* intramuscular characterization. They achieved real-time label-free detection of various muscle pathological conditions upon coupling with a machine learning model trained on over 6,000 Raman spectra of mouse models of ALS and muscular dystrophy. Groom et al. [151] developed a novel hollow-core fiber Raman probe with an integrated microlens capable of achieving spot sizes of 1.1 μm to enhance resolution limits of existing fiber-based Raman systems. Ilchenko et al. [152] developed a full capability Raman spectrometer at centimeter spatial scale by replacing bulky components in traditional Raman spectroscopy with diode lasers, densely packed optics, and compact complementary metal oxide semiconductor sensors.

6.2 Quantum light in Raman spectroscopy

Quantum-enhanced Raman microscopy exploits quantum coherence effects, including entangled photons and vibrational coherence, along with squeezed light techniques to surpass classical limits in sensitivity and spectral selectivity. Fan et al. [153] introduced a theoretical framework to evaluate the potential of entangled photons in enhancing ultrafast SRS microscopy. The work proposed that the utilization of Hong-Ou-Mandel two-photon interference effects allowed for precise tuning of photon arrival times and energy distributions, which enabled selective amplification of specific vibrational transitions, and eliminated unwanted signals from inhomogeneous line broadening from typical excitation pulses. In a work challenging the notion of incoherence in vibrational excitations associated with spontaneous Raman spectroscopy, Vento et al. [154] measured time-resolved Stokes-anti Stokes photon correlations to test for coherence (a single vibrational excited state shared across molecules) among vibrational excitations. In observing periodic oscillations in a correlation function associated with photon pair statistics, they confirmed a collective quantum coherent state, providing motivation for further development of time-resolved detection schemes with spontaneous Raman spectroscopy. Another quantum enhancement scheme surrounds the use of squeezed light, a quantum state of light with reduced uncertainty in either phase or amplitude, to surpass intrinsic shot noise limits in traditional Raman microscopy techniques. Proposing a squeezed light enhanced interferometer scheme into CARS and SRS microscopy, Michael et al. [155] predicted a greater than 6.65 dB enhancement to Raman SNR by placing a Raman sample between phase-sensitive optical parametric amplifiers to both generate squeezed light and subsequently correct incoherent non-resonant effects induced through sample interaction. In an experimental demonstration of squeezed light-enhanced SRS microscopy, Andrade et al. [156] incorporated amplitude-squeezed states of light into continuous wave SRS, surpassing the shot noise limit by demonstrating a quantum enhancement of SNR to 3.6 dB, a more than 50% improvement over conventional coherent Raman detection. More recently, Terrasson et al. [157] improved Raman microscopy sensitivity and speed by utilizing amplitude-squeezed light in single-beam SRS microscopy, surpassing the shot noise limit sensitivity, and achieving a 1.2 dB enhancement in SNR and 20% faster acquisition speed in live cell imaging compared to traditional SRS microscopy.

6.3 Time-resolved Raman spectroscopy

Advancements in time-resolved Raman spectroscopy focus on the development of experimental schemes to enable direct tracking of

ultrafast molecular dynamics in excited states. A notable early example of combining time-resolved ultrafast spectroscopy schemes with spatially resolved Raman microscopy imaging was introduced by Ploetz et al. [158] in 2007. They used broad-spectrum femtosecond white-light probe pulses with intense picosecond narrowband pump pulses to acquire full vibrational spectra upon raster scan imaging, opening the door to femtosecond-resolved vibrational interrogation of samples. Utilizing femtosecond pulses with SRS, Batignani et al. [159] selectively probed excited state vibrational dynamics with sub-picosecond temporal resolution through precise control of relative time delays between Raman and probe pulses. Demonstrating on excited state vibrational modes in cresyl violet, they determined the decay kinetics with sub-100 fs precision, which exhibits clear implications for temporal mapping of molecular relaxation pathways. In a technique that further enhances time-resolved Raman microscopy, Kuramochi et al. [160] applied impulsive SRS to track ultrafast molecular structural dynamics with precision greater than 10 fs by employing a three-pulse pump probe scheme. The technique relied on a reaction-initiating pump subsequently stimulated and probed by a pair of femtosecond pulses, and successfully imaged dynamics of protein proton transfer and charge transfer in organic semiconductors. A key bottleneck in time-resolved Raman spectroscopy is the dependence on computational modeling of vibrational spectra to interpret time domain readings of molecular dynamics. Taking aim at this limitation, Mazza et al. [161] developed an ultrafast computational algorithm to synthesize coherent Raman spectra up to a million times faster than conventional computational approaches. Employing an integral transform framework to reduce computational load, they enabled the simulation of time-resolved spectra of large polyatomic molecules previously inaccessible due to computational demands. Luo et al. [162] enhanced the spatial resolution of time-resolved molecular dynamics retrieved through these approaches by integrating them with TERS and achieved atomic-scale resolved structural dynamics of subphthalocyanine molecules at ~500 fs temporal resolution.

6.4 Multimodal integration development

Beyond the pursuit of enhanced individual Raman technologies, the integration of Raman-related microscopy with complementary imaging techniques represents a transformative approach to comprehensive biological characterization. These multimodal frameworks leverage the molecular specificity of Raman scattering alongside the unique capabilities of other imaging modalities to provide synergistic insights that overcome the limitations of any single technology, allowing for the correlation of vibrational chemical information with proteomic, lipidomic, and anatomical data for a more comprehensive understanding. To place Raman's molecular insights into a macroscopic anatomical context, a key area of development is its integration with established clinical imaging technologies. For example, a navigation system combines *in-situ* Raman spectroscopy with preoperative multiparametric MRI (mpMRI) to improve the detection of prostate cancer. By fusing molecular data from Raman with macroscopic radiomics features from mpMRI, this system has shown significantly higher accuracy in targeting tumors, providing a pathway for improved intraoperative guidance [163]. Similarly, for characterization at the mesoscale, a system combining Raman spectroscopy, fluorescence lifetime imaging (FLIM), and optical coherence tomography (OCT) has been developed [164]. This system correlates molecular information from Raman and FLIM with depth-resolved morphological data from OCT, enabling robust morpho-chemical characterization that can be compared with histopathological standards like H&E staining.

While integration with clinical imaging provides structural context, combining multiple label-free optical imaging modalities within a single microscope offers richer, co-localized data at the microscopic level. Platforms that unite nonlinear techniques such as two-photon excited fluorescence (TPEF), second-harmonic generation (SHG), and SRS can simultaneously image tissue metabolic state (endogenous fluorophores like nicotinamide adenine dinucleotide (NADH) and flavin adenine dinucleotide (FAD)), tissue extracellular matrix, and chemical composition (lipids and proteins). This approach has been used to analyze murine spinal sections, quantifying differences in collagen and lipid distribution between normal and osteoporotic bone, and it was also applied to reveal biomolecular and morphological features of diabetic kidney tissue, combining with SRH in 2D and 3D [55,165]. To add a dimension of cellular identity to this rich metabolic data, Raman-based microscopy can be paired with fluorescence-based methods. The SRS-FISH platform, for instance, merges SRS metabolic imaging with fluorescence *in situ* hybridization (FISH) to simultaneously identify the activity and phylogenetic identity of individual microbial cells, proving highly useful in high-throughput microbiome studies [166]. Similarly, the REDCAT framework integrates SRS with high-plex immunofluorescence imaging (Co-Detection-by-InDEXing (CODEX)), enabling the spatial co-analysis of metabolic activity and over 40 protein markers on the same tissue section [62]. This makes it possible to map metabolic states to specific, phenotypically defined cell types in complex tissues like human lymph nodes and lymphomas.

To further achieve a higher level of chemical specificity, combining Raman spectroscopy with mass spectrometry imaging (MSI) is a frontier path that links vibrational spectra to highly sensitive identification of specific lipid subtypes. The RaMALDI imaging workflow enables simultaneous Raman spectroscopic imaging (RSI) and MALDI-MSI on the same tissue section by using 1,5-diaminonaphthalene (DAN) matrix, achieving spatial resolutions down to 5 μm for both modalities. In brain tissue, RaMALDI successfully distinguished lipid-rich and nucleic acid-rich components while identifying specific phosphatidylcholines and sulfatides across gray and white matter [167]. However, the workflow remained analytically separate without true spatial integration, and it also lacked high spatial resolution. A recent advancement combining MALDI-MSI with an ultrafast focused light-based imaging platform (U-FLIP)-integrating two photon fluorescence (TPF), SHG, and SRS, introduced a hierarchical multimodal registration network (HiMReg) for precise spatial co-registration [168]. This enabled true spatial correlation analysis, revealing functional tissue unit (FTU)-specific metabolomic changes in bronchopulmonary dysplasia (BPD), including altered lipid distributions, reduced optical redox states, and specific collagen remodeling patterns. Moreover, the platform achieved

subcellular resolution, identifying distinct chemical clusters with decreased unsaturated fatty acid content and altered phosphatidylcholine in BPD, demonstrating how spatially co-registered multimodal analysis enables comprehensive molecular-to-morphological disease characterization.

7. Summary and outlook

Raman microscopy has evolved into a powerful technique for label-free, high-resolution chemical imaging, with advancements spanning spontaneous and coherent modalities, machine learning enhancements, and emergent roles in ultrafast molecular dynamics. This review highlights the key channels within the spectrum of technological innovations that have enhanced spectral, spatial, and temporal resolution, enabling precise biochemical classification, real-time biological imaging, and ultrafast molecular dynamics investigations. Emerging methodologies, such as quantum-enhanced Raman techniques utilizing entangled photons and squeezed light, along with miniaturized fiber-optic and spectrometer platforms, are further expanding the utility of Raman microscopy in clinical diagnostics and single-molecule biophysics. Furthermore, the integration of machine learning algorithms for spectral unmixing, feature recognition, and resolution enhancement accelerates the field's translational and research potential, filling in gaps presented by current technological bottlenecks and competition with diagnostic standards.

Looking forward, the field will likely see continued innovations and experimental realizations in quantum coherence-enhanced Raman techniques, allowing researchers to interrogate vibrational states with record-setting sensitivity and spectral selectivity. Squeezed light techniques, which have only recently demonstrated their ability to surpass shot-noise limits in Raman microscopy, will likely continue to mature. Regarding computational method-based enhancements to Raman microscopy, AI-driven Raman image analysis techniques are becoming increasingly commonplace as they play a critical role in resolving many bottlenecks in conventional Raman microscopy schema. In concert with continued technical improvements of baseline Raman imaging capabilities, computational approaches can always push these capabilities further through training on current state-of-the-art data sets. Miniaturization efforts will continue to push the boundaries of the translational capabilities of Raman microscopy modalities. Developments in time-resolved Raman spectroscopy will likely open new avenues for exploring fundamental biological questions through biomarkers associated with ultrafast molecular dynamics. Additionally, optimizing excitation and detection wavelengths toward the near-infrared "Golden Window" (~1,550–1,870 nm) could further enhance deeper tissue imaging by reducing scattering and absorption losses, enabling clearer access to subsurface biochemical information [169]. A challenge that will likely remain and cast a shadow over all the technological innovations covered in this review is the balancing of tradeoffs between speed, resolution, and sensitivity while keeping Raman imaging accessible and cost-effective. Overcoming these challenges and mitigating tradeoffs will require cross-disciplinary collaboration among physicists, chemists, engineers, and biomedical researchers who have all historically extended the capabilities of Raman microscopy.

Authors' contributions Lingyan Shi conceptualized the review and provided overall supervision. Erick Alvarado drafted the original manuscript with contributions from Zhi Li, Yajuan Li, and Lingyan Shi. All authors participated in reviewing, editing, and revising the manuscript and approved the final manuscript.

Compliance and ethics The author(s) declare that they have no conflict of interest.

Funding This work was supported by the National Institutes of Health (NIHU54DK134301, NIH R01GM149976, NIH U01AI167892, NIH R01HL170107, NIH 5R01NS111039, NIH R21NS125395, NIH R01AG086548), UCSD Startup funds, Sloan Research Fellow Award, and Scialog CZI Award.

References

1. Raman CV, Krishnan KS. A new type of secondary radiation. Nature. 1928; 121: 501–2.
2. Edwards HGM. Spectra–structure correlations in Raman spectroscopy. In: Chalmers JM, Griffiths PR, editors. Handbook of vibrational spectroscopy. Hoboken: John Wiley & Sons; 2001.
3. Movasaghi Z, Rehman S, Rehman IU. Raman spectroscopy of biological tissues. Appl Spectrosc Rev. 2007; 42: 493–541.
4. Moura CC, Tare RS, Oreffo ROC, Mahajan S. Raman spectroscopy and coherent anti-Stokes Raman scattering imaging: Prospective tools for monitoring skeletal cells and skeletal regeneration. J R Soc Interface. 2016; 13: 20160182.
5. Jones, RR, Hooper DC, Zhang L, Wolverson D, Valev VK. Raman techniques: Fundamentals and frontiers. Nanoscale Res Lett. 2019; 14: 231.
6. Dodo K, Fujita K, Sodeoka M. Raman spectroscopy for chemical biology research. J Am Chem Soc. 2022; 144: 19651–67.
7. McClung FJ, Weiner D. Measurement of Raman scattering cross sections for use in calculating stimulated Raman scattering effects. J Opt Soc Am. 1964; 54: 641–43.
8. Duncan MD, Reintjes J, Manuccia TJ. Scanning coherent anti-Stokes Raman microscope. Opt Lett. 1982; 7: 350.
9. Cheng JX, Xie XS. Coherent anti-Stokes Raman scattering microscopy: Instrumentation, theory, and applications. J Phys Chem B. 2004; 108: 827–40.
10. Freudiger CW, Min W, Saar BG, Lu S, Holtom GR, He C, et al. Label-free biomedical imaging with high sensitivity by stimulated Raman scattering microscopy. Science. 2008; 322: 1857–61.
11. Min W, Freudiger CW, Lu S, Xie XS. Coherent nonlinear optical imaging: Beyond fluorescence microscopy. Annu Rev Phys Chem. 2011; 62: 507–30.
12. Min W, Cheng JX, Ozeki Y. Theory, innovations and applications of stimulated Raman scattering microscopy. Nat Photon. 2025; 19: 803–16.
13. Chandra A, Kumar V, Garnaik UC, Dada R, Qamar I, Goel VK, et al. Unveiling the molecular secrets: A comprehensive review of Raman spectroscopy in biological research. ACS Omega. 2024; 9: 50049–63.
14. Shipp DW, Sinjab F, Notingher I. Raman spectroscopy: Techniques and applications in the life sciences. Adv Opt Photon. 2017; 9: 315–428.
15. Fan A, Alvarado E, Block A, Shi L. A mini review of quantitative optical technologies for imaging cell and tissue metabolism. Curr Opin Biomed Eng. 2025; 34: 100581.
16. Jang H, Wu S, Li Y, Li Z, Shi L. Metabolic nanoscopy enhanced by experimental and computational approaches. npj Imag. 2024; 2: 55.
17. Shi L, Villazon J. Optical imaging unveiling metabolic dynamics in cells and organisms during aging and diseases. Med X. 2025; 3: 8.
18. Unfried M, Schmauck-Medina T, Amin ND, Boyden ES, Fuellen G, Han JJ, et al. Innovations in aging biology: Highlights from the ARDD emerging science & technologies workshop. npj Aging. 2025; 11: 8.
19. Villazon JI, Jang H, Shi L. Nonlinear optical imaging modalities in biomedicine. GEN Biotechnol. 2024; 3: 290–8.
20. van Manen HJ, Lenferink A, Otto C. Noninvasive imaging of protein metabolic labeling in single human cells using stable isotopes and Raman microscopy. Anal Chem. 2008; 80: 9576–82.
21. Shi L, Zheng C, Shen Y, Chen Z, Silveira ES, Zhang L, et al. Optical imaging of metabolic dynamics in animals. Nat Commun. 2018; 9: 2995.
22. Razi S, Tarcea N, Henkel T, Ravikumar R, Pistiki A, Wagenhaus A, et al. Raman-activated, interactive sorting of isotope-labeled bacteria. Sensors. 2024; 24: 4503.
23. Yang K, Xu F, Zhu L, Li H, Sun Q, Yan A, et al. An isotope-labeled single-cell Raman spectroscopy approach for tracking the physiological evolution trajectory of bacteria toward antibiotic resistance. Angew Chem. 2023; 135: e202217412.
24. Yasuda M, Takeshita N, Shigeto S. Deuterium-labeled Raman tracking of glucose accumulation and protein metabolic dynamics in Aspergillus nidulans hyphal tips. Sci Rep. 2021; 11: 1279.
25. Yonamine Y, Asai T, Suzuki Y, Ito T, Ozeki Y, Hoshino Y. Probing the biogenesis of polysaccharide granules in algal cells at sub-organellar resolution via

Raman microscopy with stable isotope labeling. Anal Chem. 2021; 93: 16796–803.
26. Yamakoshi H, Dodo K, Palonpon A, Ando J, Fujita K, Kawata S, et al. Alkyne-tag Raman imaging for visualization of mobile small molecules in live cells. J Am Chem Soc. 2012; 134: 20681–9.
27. Wei L, Hu F, Shen Y, Chen Z, Yu Y, Lin CC, et al. Live-cell imaging of alkyne-tagged small biomolecules by stimulated Raman scattering. Nat Methods. 2014; 11: 410–2.
28. Romei MG, von Krusenstiern EV, Ridings ST, King RN, Fortier JC, McKeon CA, et al. Frequency changes in terminal alkynes provide strong, sensitive, and solvatochromic Raman probes of biochemical environments. J Phys Chem B. 2023; 127: 85–94.
29. Bi X, Miao K, Wei L. Alkyne-tagged Raman probes for local environmental sensing by hydrogen–deuterium exchange. J Am Chem Soc. 2022; 144: 8504–14.
30. Fujioka H, Shou J, Kojima R, Urano Y, Ozeki Y, Kamiya M. Multicolor activatable Raman probes for simultaneous detection of plural enzyme activities. J Am Chem Soc. 2020; 142: 20701–7.
31. de Moliner F, Knox K, Gordon D, Lee M, Tipping WJ, Geddis A, et al. A palette of minimally tagged sucrose analogues for real-time Raman imaging of intracellular plant metabolism. Angew Chem. 2021; 133: 7715–20.
32. Haes AJ, Hall WP, Chang L, Klein WL, Van Duyne RP. A localized surface plasmon resonance biosensor: First steps toward an assay for Alzheimer's disease. Nano Lett. 2004; 4: 1029–34.
33. Wang Y, Yan B, Chen L. SERS tags: Novel optical nanoprobes for bioanalysis. Chem Rev. 2013; 113: 1391–428.
34. Li J, Wu T, Wang C, Tu J, Song X, Shao Y, et al. Nanogapped Fe_3O_4@Au surface-enhanced Raman scattering tags for the multiplex detection of bacteria on an immunochromatographic strip. ACS Appl Nano Mater. 2022; 5: 12679–89.
35. Wang J, Koo KM, Trau M. Tetraplex immunophenotyping of cell surface proteomes via synthesized plasmonic nanotags and portable Raman spectroscopy. Anal Chem. 2022; 94: 14906–16.
36. Li Y, Liu X, Guo J, Zhang Y, Guo J, Wu X, et al. Simultaneous detection of inflammatory biomarkers by SERS nanotag-based lateral flow assay with portable cloud Raman spectrometer. Nanomaterials. 2021; 11: 1496.
37. Bao Z, Deng B, Zhang Y, Li X, Tan Z, Gu Z, et al. Ratiometric Raman nanotags enable intraoperative detection of metastatic sentinel lymph node. Biomaterials. 2021; 276: 121070.
38. Zhang Y, Gu Y, He J, Thackray BD, Ye J. Ultrabright gap-enhanced Raman tags for high-speed bioimaging. Nat Commun. 2019; 10: 3905.
39. Zavaleta CL, Smith BR, Walton I, Doering W, Davis G, Shojaei B, et al. Multiplexed imaging of surface enhanced Raman scattering nanotags in living mice using noninvasive Raman spectroscopy. Proc Natl Acad Sci USA. 2009; 106: 13511–6.
40. Yu JH, Steinberg I, Davis RM, Malkovskiy AV, Zlitni A, Radzyminski RK, et al. Noninvasive and highly multiplexed five-color tumor imaging of multicore near-infrared resonant surface-enhanced Raman nanoparticles *in vivo*. ACS Nano. 2021; 15: 19956–69.
41. Zhao Z, Chen C, Wei S, Xiong H, Hu F, Miao Y, et al. Ultra-bright Raman dots for multiplexed optical imaging. Nat Commun. 2021; 12: 1305.
42. Chen C, Zhao Z, Qian N, Wei S, Hu F, Min W. Multiplexed live-cell profiling with Raman probes. Nat Commun. 2012; 12: 3405.
43. Shi L, Wei M, Miao Y, Qian N, Shi L, Singer RA, et al. Highly-multiplexed volumetric mapping with Raman dye imaging and tissue clearing. Nat Biotechnol. 2022; 40: 364–73.
44. Zhang L, Shi L, Shen Y, Miao Y, Wei M, Qian N, et al. Spectral tracing of deuterium for imaging glucose metabolism. Nat Biomed Eng. 2019; 3: 402–13.
45. Borek-Dorosz A, Pieczara A, Orleanska J, Brzozowski K, Tipping W, Graham D, et al. Raman microscopy reveals how cell inflammation activates glucose and lipid metabolism. Biochim Biophys Acta BBA Mol Cell Res. 2024; 1871: 119575.
46. Li Y, Zhang W, Fung AA, Shi L. DO-SRS imaging of diet regulated metabolic activities in Drosophila during aging processes. Aging Cell. 2022; 21: e13586.
47. Li Y, Li Z, Li Y, Rhine K, Ranamukhaarachchi S, Qin S, et al. Imaging cellular metabolic rewiring with suMMIT-SRS. bioRxiv. 2025, doi: 10.1101/2025.10.10.681769.
48. Ueno H, Kato Y, Tabata KV, Noji H. Revealing the metabolic activity of persisters in mycobacteria by single-cell D_2O Raman imaging spectroscopy. Anal Chem. 2091; 91: 15171–8.
49. Kopec M, Imiela A, Abramczyk H. Monitoring glycosylation metabolism in brain and breast cancer by Raman imaging. Sci Rep. 2019; 9: 166.
50. Li Z, Sarikhani E, Prayotamornkul S, Meganathan DP, Jahed Z, Shi L. Multimodal imaging unveils the impact of nanotopography on cellular metabolic activities. Chem Biomed Imag. 2024; 2: 825–34.
51. Eremina OE, Czaja AT, Fernando A, Aron A, Eremin DB, Zavaleta C. Expanding the multiplexing capabilities of Raman imaging to reveal highly specific molecular expression and enable spatial profiling. ACS Nano. 2022; 16: 10341–53.
52. Albro MB, Bergholt MS, St-Pierre JP, Guitart AV, Zlotnick HM, Evita EG, et al. Raman spectroscopic imaging for quantification of depth-dependent and local heterogeneities in native and engineered cartilage. npj Regen Med. 2018; 3: 3.
53. Chen WW, Lemieux GA, Camp CH Jr, Chang TC, Ashrafi K, Cicerone MT. Spectroscopic coherent Raman imaging of Caenorhabditis elegans reveals lipid particle diversity. Nat Chem Biol. 2020; 16: 1087–95.
54. Ji M, Arbel M, Zhang L, Freudiger CW, Hou SS, Lin D, et al. Label-free imaging of amyloid plaques in Alzheimer's disease with stimulated Raman scattering microscopy. Sci Adv. 2018; 4: eaat7715.
55. Fung AA, Li Z, Boote C, Markov P, Gaut JP, Jain S, et al. Label-free multimodal optical biopsy reveals biomolecular and morphological features of diabetic kidney tissue in 2D and 3D. Nat Commun. 2025; 16: 4509.
56. Li Y, Zhang Z, Enninful A, Farzad N, Rajbhandari P, Nam J, et al. All-optical multimodal mapping of single cell type-specific metabolic activities via RED-CAT. bioRxiv. 2024, doi: 10.1101/2024.11.07.622511.
57. Du J, Su Y, Qian C, Yuan D, Miao K, Lee D, et al. Raman-guided subcellular pharmaco-metabolomics for metastatic melanoma cells. Nat Commun. 2020; 11: 4830.
58. Li Y, Munoz-Mayorga D, Nie Y, Kang N, Tao Y, Lagerwall J, et al. Microglial lipid droplet accumulation in tauopathy brain is regulated by neuronal AMPK. Cell Metab. 2024; 36: 1351–70.e8.
59. Abramczyk H, Brozek-Pluska B, Kopeć M. Double face of cytochrome c in cancers by Raman imaging. Sci Rep. 2022; 12: 2120.
60. Li Z, Nguyen C, Jang H, Hoang D, Min S, Ackerstaff E, et al. Multimodal imaging of metabolic activities for distinguishing subtypes of breast cancer. Biomed Opt Express. 2023; 14: 5764–80.
61. Haessler A, Candlish M, Hefendehl JK, Jung N, Windbergs M. Mapping cellular stress and lipid dysregulation in Alzheimer-related progressive neurodegeneration using label-free Raman microscopy. Commun Biol. 2024; 7: 1514.
62. Minamikawa T, Ichimura-Shimizu M, Takanari H, Morimoto Y, Shiomi R, Tanioka H, et al. Molecular imaging analysis of microvesicular and macrovesicular lipid droplets in non-alcoholic fatty liver disease by Raman microscopy. Sci Rep. 2020; 10: 18548.
63. Altangerel N, Neuman BW, Hemmer PR, Yakovlev VV, Rajil N, Yi Z, et al. Label-free drug interaction screening via Raman microscopy. Proc Natl Acad Sci USA. 2023; 120: e2218826120.
64. Tipping WJ, Merchant AS, Fearon R, Tomkinson NCO, Faulds K, Graham D. Temporal imaging of drug dynamics in live cells using stimulated Raman scattering microscopy and a perfusion cell culture system. RSC Chem Biol. 2022; 3: 1154–64.
65. LaLone V, Smith D, Diaz-Espinosa J, Rosania GR. Quantitative Raman chemical imaging of intracellular drug-membrane aggregates and small molecule drug precipitates in cytoplasmic organelles. Adv Drug Deliv Rev. 2023; 202: 115107.
66. Bae K, Zheng W, Ma Y, Huang Z. Real-time monitoring of pharmacokinetics of antibiotics in biofilms with Raman-tagged hyperspectral stimulated Raman scattering microscopy. Theranostics. 2019; 9: 1348–57.
67. Bae K, Zheng W, Ma Y, Huang Z. Real-time monitoring of pharmacokinetics of mitochondria-targeting molecules in live cells with bioorthogonal hyperspectral stimulated Raman scattering microscopy. Anal Chem. 2020; 92: 740–8.
68. Lin P, Ni H, Li H, Vickers NA, Tan Y, Gong R, et al. Volumetric chemical imaging *in vivo* by a remote-focusing stimulated Raman scattering microscope. Opt Express. 2020; 28: 30210–21.
69. Hu F, Shi L, Min W. Biological imaging of chemical bonds by stimulated Raman scattering microscopy. Nat Methods. 2019; 16: 830–42.
70. Zhang Y, Hong H, Cai W. Imaging with Raman spectroscopy. Curr Pharm Biotechnol. 2010; 11: 654–61.
71. Bi X, Czajkowsky DM, Shao Z, Ye J. Digital colloid-enhanced Raman spectroscopy by single-molecule counting. Nature. 2024; 628: 771–5.
72. Erkızan SN, İdikut F, Demirtaş Ö, Goodarzi A, Demir AK, Borra M, et al. LIPSS for SERS: Metal coated direct laser written periodic nanostructures for surface enhanced Raman spectroscopy. Adv Opt Mater. 2022; 10: 2200233.
73. Minamikawa T, Sakaguchi R, Harada Y, Tanioka H, Inoue S, Hase H, et al. Long-range enhancement for fluorescence and Raman spectroscopy using Ag nanoislands protected with column-structured silica overlayer. Light Sci Appl. 2024; 13: 299.
74. Domes R, Frosch T. Investigations on the novel antimalarial ferroquine in biomimetic solutions using deep UV resonance Raman spectroscopy and density functional theory. Anal Chem. 2023; 95: 7630–9.
75. Liang Q, Gong X, Liu J, Ke C, Dong J, Song G, et al. Ionic-wind-enhanced Raman spectroscopy without enhancement substrates. Anal Chem. 2022; 95: 1318–26.
76. Ardini B, Bassi A, Candeo A, Genco A, Trovatello C, Liu F, et al. High-throughput multimodal wide-field Fourier-transform Raman microscope. Optica. 2023; 10: 663–70.
77. Wang M, Zhang C, Yan S, Chen T, Fang H, Yuan X. Wide-field super-resolved Raman imaging of carbon materials. ACS Photonics. 2021; 8: 1801–9.
78. Grand C, Scotté C, Rigneault H. Fast compressive Raman imaging of polymorph molecules and excipients in pharmaceutical tablets. Anal Chem. 2022; 94:

16632–7.
79. Sturm B, Soldevila F, Tajahuerce E, Gigan S, Rigneault H, de Aguiar HB. High-sensitivity high-speed compressive spectrometer for Raman imaging. ACS Photonics. 2019; 6: 1409–15.
80. Guo K, Kalyviotis K, Pantazis P, Rowlands CJ. Hyperspectral oblique plane microscopy enables spontaneous, label-free imaging of biological dynamic processes in live animals. Proc Natl Acad Sci USA. 2024; 121: e2404232121.
81. Kallepitis C, Bergholt MS, Mazo MM, Leonardo V, Skaalure SC, Maynard SA, et al. Quantitative volumetric Raman imaging of three dimensional cell cultures. Nat Commun. 2017; 8: 14843.
82. LaLone V, Aizenshtadt A, Goertz J, Skottvoll FS, Mota MB, You J, et al. Quantitative chemometric phenotyping of three-dimensional liver organoids by Raman spectral imaging. Cell Rep Meth. 2023; 3: 100440.
83. Wang N, Wang X, Yan T, Xie H, Wang L, Ren F, et al. Label-free structural and functional volumetric imaging by dual-modality optical-Raman projection tomography. Sci Adv. 2023; 9: eadf3504.
84. Stepula E, Walther AR, Jensen M, Mehrotra DR, Yuan MH, Pedersen SV, et al. Label-free 3D molecular imaging of living tissues using Raman spectral projection tomography. Nat Commun. 2024; 15: 7717.
85. Ilchenko O, Pilgun Y, Kutsyk A, Bachmann F, Slipets R, Todeschini M, et al. Fast and quantitative 2D and 3D orientation mapping using Raman microscopy. Nat Commun. 2019; 10: 5555.
86. Mrđenović D, Ge W, Kumar N, Zenobi R. Nanoscale chemical imaging of human cell membranes using tip-enhanced Raman spectroscopy. Angew Chem. 2022; 134: e202210288.
87. de Albuquerque CDL, Schultz ZD. Super-resolution surface-enhanced Raman scattering imaging of single particles in cells. Anal Chem. 2020; 92: 9389–98.
88. Lee H, Kang K, Mochizuki K, Lee C, Toh KA, Lee SA, et al. Surface plasmon localization-based super-resolved Raman microscopy. Nano Lett. 2020; 20: 8951–8.
89. Liebel M, Pazos-Perez N, van Hulst NF, Alvarez-Puebla RA. Surface-enhanced Raman scattering holography. Nat Nanotechnol. 2020; 15: 1005–11.
90. Petrov GI, Arora R, Yakovlev VV, Wang X, Sokolov AV, Scully MO. Comparison of coherent and spontaneous Raman microspectroscopies for noninvasive detection of single bacterial endospores. Proc Natl Acad Sci USA. 2007; 104: 7776–9.
91. Brzozowski K, Matuszyk E, Pieczara A, Firlej J, Nowakowska AM, Baranska M. Stimulated Raman scattering microscopy in chemistry and life science–development, innovation, perspectives. Biotechnol Adv. 2022; 60: 108003.
92. Nishiyama R, Furuya K, Tamura T, Nakao R, Peterson W, Hiramatsu K, et al. Fourier transform coherent anti-stokes Raman scattering spectroscopy: A comprehensive review. Anal Chem. 2024; 96: 18322–36.
93. Sinjab F, Hashimoto K, Zhao X, Nagashima Y, Ideguchi T. Enhanced spectral resolution for broadband coherent anti-Stokes Raman spectroscopy. Opt Lett. 2020; 45: 1515–18.
94. Heuke S, Sivankutty S, Scotte C, Stockton P, Bartels RA, Sentenac A, et al. Spatial frequency modulated imaging in coherent anti-Stokes Raman microscopy. Optica. 2020; 7: 417–24.
95. Tang Q, Li B, Wang J, Liu Y, Pinkas I, Rigneault H, et al. Electronic-resonance coherent anti-Stokes Raman scattering spectroscopy and microscopy. ACS Photonics. 2024; 11: 3467–75.
96. Inoue K, Okuno M. Coherent anti-Stokes hyper-Raman spectroscopy. Nat Commun. 2025; 16: 306.
97. Lin H, Lee HJ, Tague N, Lugagne JB, Zong C, Deng F, et al. Microsecond fingerprint stimulated Raman spectroscopic imaging by ultrafast tuning and spatial-spectral learning. Nat Commun. 2021; 12: 3052.
98. Zhuge M, Huang KC, Lee HJ, Jiang Y, Tan Y, Lin H, et al. Ultrasensitive vibrational imaging of retinoids by visible preresonance stimulated Raman scattering microscopy. Adv Sci. 2021; 8: 2003136.
99. Yu Q, Yao Z, Zhou J, Yu W, Zhuang C, Qi Y, et al. Transient stimulated Raman scattering spectroscopy and imaging. Light Sci Appl. 2024; 13: 70.
100. Xiong H, Shi L, Wei L, Shen Y, Long R, Zhao Z, et al. Stimulated Raman excited fluorescence spectroscopy and imaging. Nat Photonics. 2019; 13: 412–7.
101. Zhu Y, Ge X, Ni H, Yin J, Lin H, Wang L, et al. Stimulated Raman photothermal microscopy toward ultrasensitive chemical imaging. Sci Adv. 2023; 9: eadi2181.
102. Gudavičius D, Kontenis L, Langbein W. Thousand foci coherent anti-Stokes Raman scattering microscopy. APL Photonics. 2024; 9: 086110.
103. Zong C, Cheng R, Chen F, Lin P, Zhang M, Chen Z, et al. Wide-field surface-enhanced coherent anti-Stokes Raman scattering microscopy. ACS Photonics. 2022; 9: 1042–9.
104. Lv T, Han B, Yan M, Wen Z, Huang K, Yang K, et al. Ultrahigh-speed coherent anti-Stokes Raman spectroscopy with a hybrid dual-comb source. ACS Photonics. 2023; 10: 2964–71.
105. Zhang Y, Lu M, Wu T, Chen K, Feng Y, Wang W, et al. Delay-spectral focusing dual-comb coherent Raman spectroscopy for rapid detection in the high-wavenumber region. ACS Photonics. 2022; 9: 1385–94.
106. Wu F, Li S, Chen X, Yue S, Hong W, Wang P. High-sensitive and background-free coherent anti-Stokes Raman scattering microscopy using delay modulation. Laser Photonics Rev. 2024; 18: 2300827.
107. Kong C, Pilger C, Hachmeister H, Wei X, Cheung TH, Lai CSW, et al. High-contrast, fast chemical imaging by coherent Raman scattering using a self-synchronized two-colour fibre laser. Light Sci Appl. 2020; 9: 25.
108. Li H, Cheng Y, Tang H, Bi Y, Chen Y, Yang G, et al. Imaging chemical kinetics of radical polymerization with an ultrafast coherent Raman microscope. Adv Sci. 2020; 7: 1903644.
109. Bae K, Zheng W, Huang Z. Spatial light-modulated stimulated Raman scattering (SLM-SRS) microscopy for rapid multiplexed vibrational imaging. Theranostics. 2020; 10: 312–22.
110. Ni H, Lin P, Zhu Y, Zhang M, Tan Y, Zhan Y, et al. Multiwindow SRS imaging using a rapid widely tunable fiber laser. Anal Chem. 2021; 93: 15703–11.
111. Fantuzzi EM, Heuke S, Labouesse S, Gudavičius D, Bartels R, Sentenac A, et al. Wide-field coherent anti-Stokes Raman scattering microscopy using random illuminations. Nat Photon. 2023; 17: 1097–104.
112. Karuna A, Masia F, Wiltshire M, Errington R, Borri P, Langbein W. Label-free volumetric quantitative imaging of the human somatic cell division by hyperspectral coherent anti-Stokes Raman scattering. Anal Chem. 2019; 91: 2813–21.
113. Lin P, Chen WT, Yousef KMA, Marchioni J, Zhu A, Capasso F, et al. Coherent Raman scattering imaging with a near-infrared achromatic metalens. APL Photonics. 2021; 6: 096107.
114. Xu S, Jin Y, Lee YJ. 3D orientation imaging of polymer chains with polarization-controlled coherent Raman microscopy. J Am Chem Soc. 2022; 144: 23030–43.
115. Gong L, Lin S, Huang Z. Stimulated Raman scattering tomography enables label-free volumetric deep tissue imaging. Laser Photonics Rev. 2021; 15: 2100069.
116. Lin S, Gong L, Huang Z. Time-of-flight resolved stimulated Raman scattering microscopy using counter-propagating ultraslow Bessel light bullets generation. Light Sci Appl. 2024; 13: 148.
117. Wei M, Shi L, Shen Y, Zhao Z, Guzman A, Kaufman LJ, et al. Volumetric chemical imaging by clearing-enhanced stimulated Raman scattering microscopy. Proc Natl Acad Sci USA. 2019; 116: 6608–17.
118. Moester MJB, Zada L, Fokker B, Ariese F, de Boer JF. Stimulated Raman scattering microscopy with long wavelengths for improved imaging depth. J Raman Spectrosc. 2019; 50: 1321–8.
119. Gong L, Zheng W, Ma Y, Huang Z. Higher-order coherent anti-Stokes Raman scattering microscopy realizes label-free super-resolution vibrational imaging. Nat Photonics. 2020; 14: 115–22.
120. Zhitnitsky A, Benjamin E, Bitton O, Oron D. Super-resolved coherent anti-Stokes Raman scattering microscopy by coherent image scanning. Nat Commun. 2024; 15: 10073.
121. Tomita K, Kojima Y, Kannari F. Selective coherent anti-Stokes Raman scattering microscopy employing dual-wavelength nanofocused ultrafast plasmon pulses. Nano Lett. 2018; 18: 1366–72.
122. Deckert V, Deckert-Gaudig T, Cialla-May D, Popp J, Zell R, Deinhard-Emmer S, et al. Laser spectroscopic technique for direct identification of a single virus I: FASTER CARS. Proc Natl Acad Sci USA. 2020; 117: 27820–4.
123. Burde R, Reuter N, Pruccoli A, Birech Z, Winterhalder M, Zumbusch A. Electronically preresonant coherent anti-Stokes Raman scattering microscopy. J Raman Spectrosc. 2025; 56: 939–948.
124. Lin H, Seitz S, Tan Y, Lugagne JB, Wang L, Ding G, et al. Label-free nanoscopy of cell metabolism by ultrasensitive reweighted visible stimulated Raman scattering. Nat Methods. 2025; 22: 1040–50.
125. Gong L, Zheng W, Ma Y, Huang Z. Saturated stimulated-Raman-scattering microscopy for far-field superresolution vibrational imaging. Phys Rev Appl. 2019; 11: 034041.
126. Xiong H, Qian N, Miao Y, Zhao Z, Chen C, Min W. Super-resolution vibrational microscopy by stimulated Raman excited fluorescence. Light Sci Appl. 2021; 10: 87.
127. Shou J, Komazawa A, Wachi Y, Kawatani M, Fujioka H, Spratt SJ, et al. Super-resolution vibrational imaging based on photoswitchable Raman probe. Sci Adv. 2023; 9: eade9118.
128. Shi L, Klimas A, Gallagher B, Cheng Z, Fu F, Wijesekara P, et al. Super-resolution vibrational imaging using expansion stimulated Raman scattering microscopy. Adv Sci. 2022; 9: 2200315.
129. Ao J, Fang X, Miao X, Ling J, Kang H, Park S, et al. Switchable stimulated Raman scattering microscopy with photochromic vibrational probes. Nat Commun. 2021; 12: 3089.
130. He H, Yan S, Lyu D, Xu M, Ye R, Zheng P, et al. Deep learning for biospectroscopy and biospectral imaging: State-of-the-art and perspectives. Anal Chem. 2021; 93: 3653–65.
131. Haque MIU, Lebron A, Alvarez FJD, Neal JF, Mamak M, Mukherjee D, et al. Deep learning-driven super-resolution in Raman hyperspectral imaging: Efficient high-resolution reconstruction from low-resolution data. Appl Phys Lett. 2024; 125: 204104.
132. He H, Xu M, Zong C, Zheng P, Luo L, Wang L, et al. Speeding up the line-scan Raman imaging of living cells by deep convolutional neural network. Anal Chem.

2019; 91: 7070–7.
133. Jang H, Li Y, Fung AA, Bagheri P, Hoang K, Skowronska-Krawczyk D, et al. Super-resolution SRS microscopy with A-PoD. Nat Methods. 2023; 20: 448–58.
134. He H, Cao M, Gao Y, Zheng P, Yan S, Zhong JH, et al. Noise learning of instruments for high-contrast, high-resolution and fast hyperspectral microscopy and nanoscopy. Nat Commun. 2024; 15: 754.
135. Hu J, Chen GJ, Xue C, Liang P, Xiang Y, Zhang C, et al. RSPSSL: A novel high-fidelity Raman spectral preprocessing scheme to enhance biomedical applications and chemical resolution visualization. Light Sci Appl. 2024; 13: 52.
136. Valensise, CM, Giuseppi A, Vernuccio F, De la Cadena A, Cerullo G, Polli D. Removing non-resonant background from CARS spectra via deep learning. APL Photonics. 2020; 5: 061305.
137. Zhang Q, Yun KK, Wang H, Yoon SW, Lu F, Won D. Automatic cell counting from stimulated Raman imaging using deep learning. PLoS One. 2021; 16: e0254586.
138. Lu S, Huang Y, Shen WX, Cao YL, Cai M, Chen Y, et al. Raman spectroscopic deep learning with signal aggregated representations for enhanced cell phenotype and signature identification. PNAS Nexus. 2024; 3: pgae268.
139. Liu Z, Su W, Ao J, Wang M, Jiang Q, He J, et al. Instant diagnosis of gastroscopic biopsy via deep-learned single-shot femtosecond stimulated Raman histology. Nat Commun. 2022; 13: 4050.
140. Hollon TC, Pandian B, Adapa AR, Urias E, Save AV, Khalsa SSS, et al. Near real-time intraoperative brain tumor diagnosis using stimulated Raman histology and deep neural networks. Nat Med. 2020; 26: 52–8.
141. Kondepudi A, Pekmezci M, Hou X, Scotford K, Jiang C, Rao A, et al. Foundation models for fast, label-free detection of glioma infiltration. Nature. 2025; 637: 439–45.
142. Liu Z, Chen L, Cheng H, Ao J, Xiong J, Liu X, et al. Virtual formalin-fixed and paraffin-embedded staining of fresh brain tissue via stimulated Raman CycleGAN model. Sci Adv. 2024; 10: eadn3426.
143. Ye J, Yeh YT, Xue Y, Wang Z, Zhang N, Liu H, et al. Accurate virus identification with interpretable Raman signatures by machine learning. Proc Natl Acad Sci USA. 2022; 119: e2118836119.
144. Parlatan U, Ozen MO, Kecoglu I, Koyuncu B, Torun H, Khalafkhany D, et al. Label-free identification of exosomes using Raman spectroscopy and machine learning. Small. 2023; 19: 2205519.
145. Georgiev D, Fernández-Galiana Á, Pedersen SV, Papadopoulos G, Xie R, Stevens MM, et al. Hyperspectral unmixing for Raman spectroscopy via physics-constrained autoencoders. Proc Natl Acad Sci USA. 2024; 121: e2407439121.
146. Zhang W, Li Y, Fung AA, Li Z, Jang H, Zha H, et al. Multi-molecular hyperspectral PRM-SRS microscopy. Nat Commun. 2024; 15: 1599.
147. Ju Y, Neumann O, Bajomo M, Zhao Y, Nordlander P, Halas NJ, et al. Identifying surface-enhanced Raman spectra with a Raman library using machine learning. ACS Nano. 2023; 17: 21251–61.
148. Lin SJ, Chao PH, Cheng HW, Wang JK, Wang YL, Han YY, et al. An antibiotic concentration gradient microfluidic device integrating surface-enhanced Raman spectroscopy for multiplex antimicrobial susceptibility testing. Lab Chip. 2022; 22: 1805–14.
149. Žuvela P, Lin K, Shu C, Zheng W, Lim CM, Huang Z. Fiber-optic Raman spectroscopy with nature-inspired genetic algorithms enhances real-time *in vivo* detection and diagnosis of nasopharyngeal carcinoma. Anal Chem. 2019; 91: 8101–8.
150. Plesia M, Stevens OA, Lloyd GR, Kendall CA, Coldicott I, Kennerley AJ, et al. *In vivo* fiber optic Raman spectroscopy of muscle in preclinical models of amyotrophic lateral sclerosis and Duchenne muscular dystrophy. ACS Chem Neurosci. 2021; 12: 1768–76.
151. Groom MJ, Miele E, Pinnell J, Ellis MG, McConnell JB, Sakr H, et al. Microlens hollow-core fiber probes for operando Raman spectroscopy. ACS Photonics. 2024; 11: 3167–77.
152. Ilchenko O, Pilhun Y, Kutsyk A, Slobodianiuk D, Goksel Y, Dumont E, et al. Optics miniaturization strategy for demanding Raman spectroscopy applications. Nat Commun. 2024; 15: 3049.
153. Fan JJ, Ou ZY, Zhang Z. Entangled photons enabled ultrafast stimulated Raman spectroscopy for molecular dynamics. Light Sci Appl. 2024; 13: 163.
154. Vento V, Tarrago Velez S, Pogrebna A, Galland C. Measurement-induced collective vibrational quantum coherence under spontaneous Raman scattering in a liquid. Nat Commun. 2023; 14: 2818.
155. Michael Y, Bello L, Rosenbluh M, Pe'er A. Squeezing-enhanced Raman spectroscopy. npj Quantum Inf. 2019; 5: 81.
156. de Andrade RB, Kerdoncuff H, Berg-Sørensen K, Gehring T, Lassen M, Andersen UL. Quantum-enhanced continuous-wave stimulated Raman scattering spectroscopy. Optica. 2020; 7: 470–5.
157. Terrasson A, Mauranyapin NP, Casacio CA, Grim JQ, Barnscheidt K, Hage B, et al. Fast biological imaging with quantum-enhanced Raman microscopy. Opt Express. 2024; 32: 36193–206.
158. Ploetz E, Laimgruber S, Berner S, Zinth W, Gilch P. Femtosecond stimulated Raman microscopy. Appl Phys B. 2007; 87: 389–93.
159. Batignani G, Ferrante C, Scopigno T. Accessing excited state molecular vibrations by femtosecond stimulated Raman spectroscopy. J Phys Chem Lett. 2020; 11: 7805–13.
160. Kuramochi H, Tahara T. Tracking ultrafast structural dynamics by time-domain Raman spectroscopy. J Am Chem Soc. 2021; 143: 9699–717.
161. Mazza F, van den Bekerom D. An ultrafast algorithm for ultrafast time-resolved coherent Raman spectroscopy. Commun Chem. 2025; 8: 3.
162. Luo Y, Martin-Jimenez A, Gutzler R, Garg M, Kern K. Ultrashort pulse excited tip-enhanced Raman spectroscopy in molecules. Nano Lett. 2022; 22: 5100–6.
163. Grajales D, Picot F, Shams R, Dallaire F, Sheehy G, Alley S, et al. Image-guided Raman spectroscopy navigation system to improve transperineal prostate cancer detection. Part 2: *In-vivo* tumor-targeting using a classification model combining spectral and MRI-radiomics features. J Biomed Opt. 2022; 27: 095004.
164. Vasquez D, Knorr F, Hoffmann F, Ernst G, Marcu L, Schmitt M, et al. Multimodal scanning microscope combining optical coherence tomography, Raman spectroscopy and fluorescence lifetime microscopy for mesoscale label-free imaging of tissue. Anal Chem. 2021; 93: 11479–87.
165. Talone B, Bresci A, Manetti F, Vernuccio F, De la Cadena A, Ceconello C, et al. Label-free multimodal nonlinear optical microscopy reveals features of bone composition in pathophysiological conditions. Front Bioeng Biotechnol. 2022; 10: 1042680.
166. Ge X, Pereira FC, Mitteregger M, Berry D, Zhang M, Hausmann B, et al. SRS-FISH: A high-throughput platform linking microbiome metabolism to identity at the single-cell level. Proc Natl Acad Sci USA. 2022; 119: e2203519119.
167. Yang E, Kim JH, Tressler CM, Shen XE, Brown DR, Johnson CC, et al. RaMALDI: Enabling simultaneous Raman and MALDI imaging of the same tissue section. Biosens Bioelectron. 2023; 239: 115597.
168. Gorman BL, Li Z, Deutsch G, Huyck HL, Beishembieva N, Olson H, Villazon J, et al. A multimodal imaging approach for imaging the metabolic changes resulting from bronchopulmonary dysplasia. bioRxiv. 2025, doi: 10.1101/2025.06.16.660017.
169. Shi L, Sordillo LA, Rodríguez-Contreras A, Alfano R. Transmission in near-infrared optical windows for deep brain imaging. J Biophotonics. 2016; 9: 38–43.